

Perpendicular Magnetic Anisotropy in Conducting NiCo₂O₄ Films from Spin-Lattice Coupling

Corbyn Mellinger¹, Jace Waybright^{1,2}, Xiaozhe Zhang^{1,3}, Caleb Schmidt¹, and Xiaoshan Xu^{1,4}

¹ Department of Physics and Astronomy, University of Nebraska, Lincoln, Nebraska 68588, USA

² Department of Physics, South Dakota State University, Brookings, SD 57007 USA

³ School of Materials Science and Engineering, Xi'an Polytechnic University, Xi'an 710049, Xi'an, China

⁴ Nebraska Center for Materials and Nanoscience, University of Nebraska, Lincoln, Nebraska 68588, USA

Abstract

High perpendicular magnetic anisotropy (PMA), a property needed for nanoscale spintronic applications, is rare in oxide conductors. We report the observation of a PMA up to 0.23 MJ/m³ in modestly strained (−0.3%) epitaxial NiCo₂O₄ (NCO) films which are room-temperature ferrimagnetic conductors. Spin-lattice coupling manifested as magnetoelastic effect was found as the origin of the PMA. The in-plane x^2-y^2 states of Co on tetrahedral sites play crucial role in the magnetic anisotropy and spin-lattice coupling with an energy scale of 1 meV/f.u. The elucidation of the microscopic origin paves a way for engineering oxide conductors for PMA using metal/oxygen hybridizations.

Materials and heterostructures of high magnetic anisotropy have been increasingly demanded for energy and information applications. In particular, electrodes with perpendicular magnetic anisotropy (PMA) is needed in nanoscale spintronic devices for their high thermal stability and energy-efficient switching. Most materials or heterostructures of high PMA are based on intermetallic compounds [1–5], multilayers [6,7], or metal/oxide interfaces [8], often with high-cost elements such as Au and Pt. In contrast, transition-metal oxide conductors, despite their advantage of low-cost and structural and chemical stabilities, have rarely been reported to exhibit high PMA.

High magnetic anisotropy originates from structural anisotropy and spin-orbit coupling. In ordered intermetallic compounds containing strongly spin-orbit coupled nonmagnetic (NM) metals (e.g. Pd, Au, and Pt) and ferromagnetic (FM) metals (e.g. Fe and Co), anisotropic crystal structures lead to anisotropic hybridization between the states in NM and FM and consequently high magnetic anisotropy ($\approx 5 \text{ MJ/m}^3$) [1–5,9]. The structural anisotropy can also be introduced by stacking NM and FM layers for high PMA ($\approx 1 \text{ MJ/m}^3$) [7]. On the other hand, remarkable PMA has been demonstrated in Co/Ni multilayers ($\approx 0.5 \text{ MJ/m}^3$) [6] and FM/oxide interfaces ($\approx 0.2 \text{ MJ/m}^3$) [8,10,11], without the need of the strongly spin-orbit coupled NM. Here, the electronic degeneracy and occupancy are adjusted such that, the 3d states in FM with a large orbital angular momentum (in-plane states) determine the magnetic anisotropy. In particular, at the FM/oxide interface, the 3d electronic states are tuned via the hybridization with oxygen states; this suggests the possibility of having transition-metal oxide with high magnetic anisotropy.

In 3d transition-metal oxides, the hybridization of metal 3d and oxygen 2p states generates a crystal-field splitting $\Delta \sim 1 \text{ eV}$; the spin-orbit coupling ($\xi \sim 50 \text{ meV}$) couples these split states and modifies the energy by $\approx \langle L_z \rangle \xi^2 / \Delta$, where $\langle L_z \rangle$ is the average angular momentum projection along the out-of-plane direction. This energy modification, which gives rise to magnetic anisotropy energy, could reach $\sim 1 \text{ meV}$ if $\langle L_z \rangle \sim 1$; this is why CoFe_2O_4 , an insulator, indeed exhibits large magnetic anisotropy ($\sim 1 \text{ MJ/m}^3$) and strong spin-lattice coupling, which can be employed to realize PMA in strained films [10,12–22]. For oxide conductors, however, room temperature ferromagnetism is already rare, not to mention high magnetic anisotropy. Widely studied FM oxide conductors, such as $\text{La}_{0.7}\text{Sr}_{0.3}\text{MnO}_3$, unfortunately have low magnetic anisotropy and weak spin lattice coupling due to the dominant z^2 state which has a low orbital angular momentum [23].

Inverse spinel NiCo_2O_4 (NCO) has recently been demonstrated to be conducting due to the mixed valence [24,25], and ferrimagnetic [24,26–28] from the antialignment of Ni and Co moments above room temperature. In this work, we demonstrate that NCO has a remarkable magnetic anisotropy and spin-lattice coupling which can be employed to generate PMA up to 0.23 MJ/m^3 with a -0.3% epitaxial strain [Fig. 1]. Analysis of the microscopic origin of the magnetic anisotropy and the spin-lattice coupling based on single-ion anisotropy reveals the key role of the x^2-y^2 states in Co atoms on the tetrahedra sites.

Pulsed laser deposition (PLD) was employed to grow epitaxial NCO films between 15 and 20 nm on (001), (110), and (111)-oriented nonmagnetic MgAl_2O_4 (MAO) substrates ($a = 8.089 \text{ \AA}$ for MAO, 8.114 \AA for NCO, in-plane strain $e_{\text{in}} = -0.3\%$). Film growth was conducted with 20 mTorr O_2 pressure, $360 \text{ }^\circ\text{C}$ substrate temperature, 5 cm target-to-substrate distance, using a KrF excimer

laser (248 nm, 10 Hz, and 2.5 J/cm²). Post-growth annealing was carried out *ex-situ* in 1 atmosphere O₂ at 500 °C. The crystallinity, thickness, and lattice constants of the films were measured using x-ray diffraction (XRD) with a Rigaku D/Max-B x-ray diffractometer ($\lambda = 1.789$ Å) and a Rigaku SmartLab x-ray diffractometer ($\lambda = 1.54$ Å). The dependences of magnetization on temperature and magnetic field were measured in a Quantum Design MPMS system. In-plane magnetic anisotropy of NCO (111) films was studied using a home-built Magneto-optical Kerr Effect (MOKE) system at room temperature in a longitudinal configuration with a rotational sample stage [see Supplementary Materials].

X-ray diffraction shows an epitaxial growth of NCO (001) film on MAO (001) substrates with no observable impurity phases [Fig. 2(a)]. The Laue oscillations around the (004) peak suggest a high film quality and a thickness of 17 nm for the displayed film. Reciprocal space mapping [Fig. 2(b)] indicate that the film is fully strained since the in-plane lattice constants of the NCO film coincide with that of the MAO substrate. The NCO peak positions in Fig. 2(a) and that in Fig. 2(b) indicate an out-of-plane strain $e_{out} = 1.3\%$. For the (110) and (111) oriented films of similar thickness, e_{out} is 0.8% and 0.6%, respectively [see Supplementary Materials].

Temperature dependence of the magnetization (M-T) measured while cooling in a 100 Oe out-of-plane magnetic field shows an upturn [Fig. 2(c)], indicating a transition to magnetic ordering at $T_C = 323$ K. Figure 2(d) shows a clear square magnetization-field (M-H) hysteresis loops at 150 K, with an out-of-plane magnetic field (along the [001] axis); the coercivity is 450 Oe and the remnant magnetization is 94% of the saturation value. In contrast, the M-H relation has no significant remanence and no measurable coercivity with an in-plane field (along the [100] or [010] axes); the saturation field is 20 kOe. The distinct in-plane and out-of-plane M-H relations reveal PMA in the NCO (001) films, where [001] is the easy axis. By comparing the M-H relations with in-plane and out-of-plane magnetic fields, one can extract the anisotropy energy K_u for the PMA of NCO (001) [Fig. 1].

The PMA in the NCO (001) films, can be understood as a result of spin-lattice coupling and the broken cubic symmetry due to the biaxial epitaxial strain. On a phenomenological level, spin-lattice coupling can be described as magnetoelastic effect with the Landau theory using free energy

$$F = K_1(\alpha_1^2\alpha_2^2 + \alpha_2^2\alpha_3^2 + \alpha_3^2\alpha_1^2) + B_1(\alpha_1^2e_{xx} + \alpha_2^2e_{yy} + \alpha_3^2e_{zz}) + B_2(\alpha_1\alpha_2e_{xy} + \alpha_2\alpha_3e_{yz} + \alpha_3\alpha_1e_{zx}) \quad (1),$$

where K_1 is the magnetic anisotropy constant, α_1 , α_2 , and α_3 are the directional cosines of the magnetization with respect to x , y , and z axes respectively ($\sum\alpha_i^2 = 1$), e_{ij} are components of the strain tensor, B_1 and B_2 are the longitudinal and shear magnetoelastic coupling constants respectively. The first term in Eq. (1) corresponds to the magnetic anisotropy of cubic symmetry, while the second and third terms described the magnetoelastic coupling. Without strain ($e_{ij} = 0$), if $K_1 > 0$, by minimizing F , one finds that the global easy axes are [100], [010], and [001], which are equivalent under the cubic symmetry [see Supplementary]; the global hard axes are along [111] axis or its equivalent. These results can be visualized in Fig. 2(e), where the easy (hard) axes correspond to the energy minima (maxima).

For the NCO/MAO (001) films (nonzero strain: $e_{xx} = e_{yy} = e_{in} < 0$, $e_{zz} = e_{out} > 0$), the free energy along the [100] and [001] axis are $F_{[100]} = B_1 e_{xx}$ and $F_{[001]} = B_1 e_{zz}$, respectively; the observed easy axis along the [001] direction [Fig. 2(d)] requires $F_{[001]} < F_{[100]}$ or $B_1 < 0$, as illustrated in Fig. 2(f).

To fully characterize the magnetic anisotropy and the magnetoelastic effect, we also studied the M - H relations for the (111) and (110)-oriented NCO films.

The M - H relation of the NCO (111) films with in-plane and out-of-plane field directions, all show an “S” shaped loop with a small remanence (12%-15%) and coercivity (700 Oe along [111]; 500 Oe along other directions) [Fig. 3(a)], indicating that they are not easy axes. The easy axis is most likely tilted with non-zero projections in both in-plane and out-of-plane directions. To investigate the tilted easy axes, we carried out MOKE measurement using the longitudinal mode, which measures the projection of magnetization in the direction of the reflected light. Using this method, one may observe a normal or an inverse M - H hysteresis loop, when the in-plane azimuthal angle between the easy axis and the reflected light are less than or greater than $\pi/2$, respectively (see Supplementary Materials). As shown in Fig. 3(b), both normal and inverse M - H loops were observed when the film was rotated about the [111] axis. Using a negative coercivity to distinguish the inverse M - H loops from the normal ones, the in-plane anisotropy can be visualized using the polar plot of the coercivity [Fig. 3(b)], where the larger coercivity means closer to the easy axis. A triangular symmetry is revealed, and the in-plane projection of the easy axis appears to be along the [11-2] (or equivalent) directions. The [100], [010], and [001] directions satisfy the geometric symmetry for the easy axes observed in Fig. 3(b).

For the NCO/MAO (111) films, the nonzero strain is $e_{xy} = e_{yz} = e_{zx} = -e_{in} > 0$. According to Eq. (1), a positive (negative) B_2 suggests that the compressive strain increases (decreases) the energy of the [111] axis. Experimentally, the measured hysteresis along the out-of-plane direction [111] and the in-plane directions $[11\bar{2}]$ are similar [Fig. 3(a)], suggesting that the energy of the [111] direction is reduced from the global maximum, indicating that $B_2 < 0$. The free energies of the [100], [010], and [001] axes are not affected since all the longitudinal strains (e_{xx} , e_{yy} , and e_{zz}) are zero. For small strain, the global easy axes remain close to these directions, consistent with the MOKE observation [see Supplementary Materials].

The M - H relation of the NCO (110) films exhibits a slightly canted shape with a coercivity of 550 Oe and remnant magnetization 91% of saturation magnetization when the magnetic field is along the [100] in-plane direction. In contrast, when the magnetic field is along the in-plane [1-10] and out-of-plane [110] directions, the M - H relation has a minimal hysteresis with a saturation field 10 kOe. For the NCO/MAO (110) films, the nonzero strain is $e_{xx} = e_{yy} = (e_{in} + e_{out})/2 > 0$, $e_{zz} = e_{in} < 0$, and $e_{xy} = (e_{out} - e_{in})/2 > 0$. The free energies of the [100] and [010] axes reduce, while that of [001] axis increases, because $B_1 < 0$. Therefore, [001] becomes a local easy axis, consistent with slightly canted M - H loop measured when the field is along the in-plane [001] axis, while the global easy axes remain close to the [100] and [010] directions [see Supplementary Materials].

One may determine K_1 , B_1 , and B_2 from the magnetic anisotropy energy extracted from the M - H relations for the NCO films of different orientations. The results are listed in Table I, as well as in

Fig. 1. The tunability of the magnetic anisotropy is highlighted by the large magnetoelastic coupling coefficients B_1 and B_2 .

Next, we analyze the microscopic origin of the spin-lattice coupling in terms of the effect of strain on the single-ion magnetic anisotropy energy via the spin-orbit coupling. We employ a model Hamiltonian using a one-electron picture

$$H = \sum_i \left[\frac{p_i^2}{2m} - \frac{Ze}{4\pi\epsilon_0 r_i} + V_{CF} + \xi \vec{S}_i \cdot \vec{l}_i + E_{ex} \vec{S}_i \cdot \hat{B}_{ex} \right],$$

where p_i , l_i , S_i , \vec{r}_i are momentum, orbital angular momentum, spin, and position vector of the i th electron, $-\frac{Ze}{4\pi\epsilon_0 r_i}$ and $V_{CF}(\vec{r}_i)$ are the potential energy due to the ion core and the crystal field respectively, \hat{B}_{ex} is an exchange field that generates the energy gap E_{ex} between spins of opposite directions, e , m , ϵ_0 , g , \hbar are the electronic charge, electronic mass, vacuum permittivity, Landé g -factor, and reduced Planck constant. The spin-lattice coupling can be understood as that the strain modifies the electronic orbital states by changing the local environment of the magnetic ions (V_{CF}), followed by the change of their preferred spin orientations due to the spin-orbit coupling.

In the unit cell of NCO, eight low-spin $\text{Ni}^{3-\delta}$ ions and eight high-spin $\text{Co}^{2+\delta}$ ions are in NiO_6 octahedra [Figs. 4(a), O_h symmetry] and CoO_4 tetrahedra [Fig. 4(b), T_d symmetry] respectively, where $\delta < 1$ which indicates the mixed valences [24,25]. The other eight CoO_6 octahedra are contain low-spin Co^{3+} , which do not contribute to magnetism. The Co and Ni 3d states are split into doubly degenerate e_g states and triply degenerate t_{2g} states due to the corresponding V_{CF} . Under the biaxial compressive strain which reduces the cubic symmetry to tetragonal, these states further split [Fig. 4(a) and 4(b)].

We simulate the crystal field by replacing the oxygen atoms with point charges in NiO_6 and CoO_4 . The total energy on a magnetic ion E_t is calculated by summing the energy of the individual electrons [6] according to the population in Figs. 4(a) and (b), where $\delta=0.5$ is assumed. The single-ion magnetic anisotropy manifests in the dependence of E_t on the direction of \hat{B}_{ex} . As an example, for in the (001) NCO films, the single-ion magnetic anisotropy is defined as $E_{\text{SIMA}} = E_{t,x} - E_{t,z}$, where $E_{t,x}$ and $E_{t,z}$ are E_t when \hat{B}_{ex} is along the x (in-plane) and z (out-of-plane) axes respectively. The epitaxial strain $\Delta a/a$, where a is the bulk lattice constant, is introduced by distorting the NiO_6 and CoO_4 local environment according to the lattice constant change, which are Δa and $-2\Delta a$ for in-plane and out-of-plane axes, respectively. The simulated E_{SIMA} as a function of strain is shown in Fig. 4(c). For both $\text{Ni}^{3-\delta}$ and $\text{Co}^{2+\delta}$, under the compressive strain ($\Delta a < 0$) which generates a tetragonal distortion, E_{SIMA} is positive, suggesting that the c axis (out-of-plane direction) is the easy axis, which is consistent with the experimental observation.

To reveal more microscopic detail of the effect of strain on magnetic anisotropy, here we analyze $\text{Co}^{2+\delta}\text{O}_4$ tetrahedra as an example since it shows a larger effect in Fig. 4(c). In this case, the 3d electronic configuration can be viewed as a half-filled shell plus an electron in the $|x^2-y^2\rangle$ state and a fractional occupation in the z^2 state, due to the tetragonal distortion that generates an S_4 symmetry, as shown in Fig. 4(b) and 4(d). Since the half-filled shell is not expected to contribute to the magnetic anisotropy, the electron in the $|x^2-y^2\rangle$ state dominates the anisotropy. As illustrated

in Fig. 4(d), if the spin is along the z axis, the $|x^2-y^2, S_z=1/2\rangle$ state couples to the $|xy, S_z=1/2\rangle$ state to lower its energy with a coupling strength $\langle x^2-y^2, S_z=1/2 | \xi \vec{S}_i \cdot \vec{l}_i | xy, S_z=1/2 \rangle = \xi$. On the other hand, when the spin is along the x axis, the $|x^2-y^2, S_x=1/2\rangle$ state couples to the $|xz, S_x=1/2\rangle$ state to lower its energy with a coupling strength $\langle x^2-y^2, S_x=1/2 | \xi \vec{S}_i \cdot \vec{l}_i | xz, S_x=1/2 \rangle = \xi/2$, which is smaller than that when the spin is along the c axis. Therefore, the compressive strain results in an out-of-plane magnetic anisotropy. Hence, the 3d $|x^2-y^2\rangle$ state of Co in the $\text{Co}^{2+\delta}\text{O}_4$, plays a key role in the spin-lattice coupling of NCO due to its potentially large orbital angular momentum along the z axis. Assuming the magnitude of ξ , V_{CF} , and E_{ex} as 0.05, 1 and 5 eV respectively, the single-ion magnetic anisotropy is found to be ~ 1 meV per formula unit, as show in Fig. 4(c); this translates to ~ 1 MJ/m³ in magnetic anisotropy energy, in fair agreement with the observed values in Table I.

In conclusion, we have demonstrated a remarkable PMA in the (001)-oriented NCO/MAO epitaxial films above room temperature which can be understood as a result of the spin-lattice coupling manifested as magnetoelastic effect. The microscopic origin of spin-lattice coupling has been explained using the effect of strain on the single-ion magnetic anisotropy energy due to spin-orbit coupling. The demonstration and elucidation of the strong tunability of magnetic anisotropy in NCO, indicate the possibility of high PMA in oxide conductors. This adds material structures, such as NCO/MAO/NCO tunnel junction of enhanced magnetoresistance [29] into nanoscale spintronic devices. In addition, it opens up another route toward electrical and mechanical control of magnetism above room temperature.

Acknowledgments

This project was primarily supported by the National Science Foundation (NSF), DMR under award DMR-1454618. C.S. acknowledges the support by the Nebraska Center for Energy Sciences Research on magnetic imaging. J.W. acknowledges the support of REU program of Nebraska Center for Materials and Nanoscience on magneto optical studies. The research was performed in part in the Nebraska Nanoscale Facility: National Nanotechnology Coordinated Infrastructure, and the Nebraska Center for Materials and Nanoscience, which are supported by the National Science Foundation under award ECCS: 1542182, and the Nebraska Research Initiative.

References

- [1] B. Tudu and A. Tiwari, *Vacuum* **146**, 329 (2017).
- [2] R. Sbiaa, H. Meng, and S. N. Piramanayagam, *Phys. Status Solidi - Rapid Res. Lett.* **5**, 413 (2011).
- [3] A. Sakuma, *J. Phys. Soc. Japan* **63**, 3053 (1994).
- [4] H. O. Daalderop and H. Schuurmans, *Phys. Rev. B* **44**, 12054 (1991).
- [5] A. B. Shick and O. N. Mryasov, *Phys. Rev. B* **67**, 172407 (2003).
- [6] G. H. O. Daalderop, P. J. Kelly, and F. J. A. den Broeder, *Phys. Rev. Lett.* **68**, 682 (1992).
- [7] P. F. Carcia, *J. Appl. Phys.* **63**, 5066 (1988).
- [8] B. Dieny and M. Chshiev, *Rev. Mod. Phys.* **89**, 025008 (2017).
- [9] J. M. D. Coey, *Magnetism and Magnetic Materials* (Cambridge University Press, Cambridge, 2010).
- [10] F. Eskandari, S. B. Porter, M. Venkatesan, P. Kameli, K. Rode, and J. M. D. Coey, *Phys. Rev. Mater.* **1**, 074413 (2017).
- [11] S. Ikeda, K. Miura, H. Yamamoto, K. Mizunuma, H. D. Gan, M. Endo, S. Kanai, J. Hayakawa, F. Matsukura, and H. Ohno, *Nat. Mater.* **9**, 721 (2010).
- [12] D. Fritsch and C. Ederer, *Phys. Rev. B* **82**, 104117 (2010).
- [13] A. Raghunathan, I. C. Nlebedim, D. C. Jiles, and J. E. Snyder, *J. Appl. Phys.* **107**, 09A516 (2010).
- [14] J. Inoue, T. Niizeki, H. Yanagihara, H. Itoh, and E. Kita, *AIP Adv.* **4**, 027111 (2014).
- [15] B. H. Liu and J. Ding, *Appl. Phys. Lett.* **88**, 042506 (2006).
- [16] T. Niizeki, Y. Utsumi, R. Aoyama, H. Yanagihara, J. Inoue, Y. Yamasaki, H. Nakao, K. Koike, and E. Kita, *Appl. Phys. Lett.* **103**, 162407 (2013).
- [17] A. Lisfi and C. M. Williams, *J. Appl. Phys.* **93**, 8143 (2003).
- [18] A. Lisfi, C. M. Williams, L. T. Nguyen, J. C. Lodder, A. Coleman, H. Corcoran, A. Johnson, P. Chang, A. Kumar, and W. Morgan, *Phys. Rev. B* **76**, 054405 (2007).
- [19] W. Huang, J. Zhu, H. Z. Zeng, X. H. Wei, Y. Zhang, and Y. R. Li, *Appl. Phys. Lett.* **89**, 262506 (2006).
- [20] X. S. Gao, D. H. Bao, B. Birajdar, T. Habisreuther, R. Mattheis, M. A. Schubert, M. Alexe, and D. Hesse, *J. Phys. D: Appl. Phys.* **42**, 175006 (2009).
- [21] W. H. Wang and X. Ren, *J. Cryst. Growth* **289**, 605 (2006).
- [22] A. V. Ramos, T. S. Santos, G. X. Miao, M. J. Guittet, J. B. Moussy, and J. S. Moodera, *Phys. Rev. B* **78**, 180402 (2008).

- [23] Z. Xiao, F. Zhang, M. A. Farrukh, R. Wang, G. Zhou, Z. Quan, and X. Xu, *J. Mater. Sci.* **54**, 9017 (2019).
- [24] Y. Bitla, Y. Chin, J.-C. Lin, C. N. Van, R. Liu, Y. Zhu, H. Liu, Q. Zhan, H. Lin, C. Chen, Y. Chu, and Q. He, *Sci. Rep.* **5**, 15201 (2015).
- [25] C. Zhen, X. Zhang, W. Wei, and W. Guo, *J. Phys. D. Appl. Phys.* **51**, 145308 (2018).
- [26] X. Chen, X. Zhang, M. Han, L. Zhang, Y. Zhu, X. Xu, and X. Hong, *Adv. Mater.* **31**, 1805260 (2018).
- [27] P. Silwal, C. La-o-vorakiat, E. E. M. Chia, D. H. Kim, and D. Talbayev, *AIP Adv.* **3**, 092116 (2013).
- [28] P. Silwal, L. Miao, J. Hu, L. Spinu, D. Ho Kim, and D. Talbayev, *J. Appl. Phys.* **114**, 103704 (2013).
- [29] H. Sukegawa, Y. Miura, S. Muramoto, S. Mitani, T. Niizeki, T. Ohkubo, K. Abe, M. Shirai, K. Inomata, and K. Hono, *Phys. Rev. B* **86**, 184401 (2012).

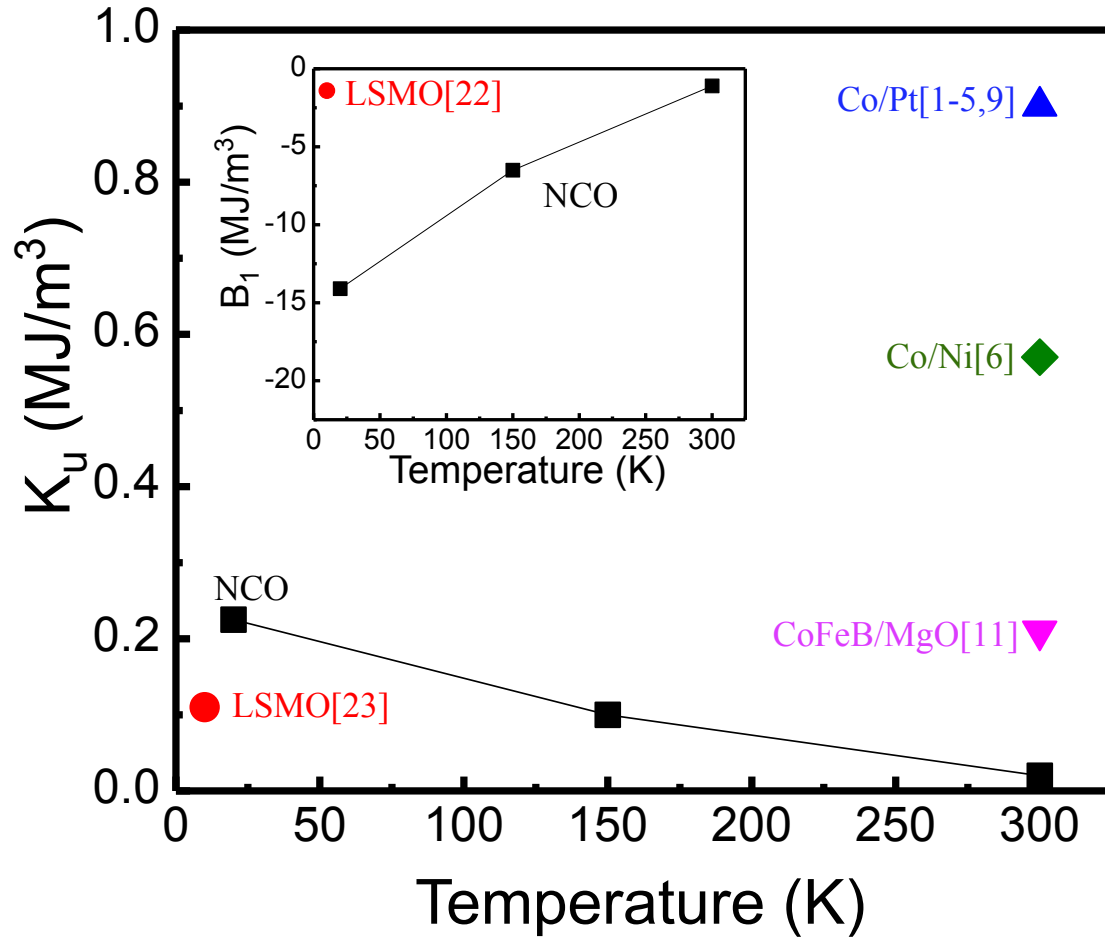


Figure 1. Uniaxial magnetic anisotropy energy K_u of strained NiCo_2O_4 (-0.3%) and $\text{La}_{0.7}\text{Sr}_{0.3}\text{MnO}_3$ (-2.1%) films, Co/Pt and Co/Ni multilayers, and CoFeB/MgO heterostructures. Inset: magnetoelastic coupling coefficient B_1 of NiCo_2O_4 and $\text{La}_{0.7}\text{Sr}_{0.3}\text{MnO}_3$.

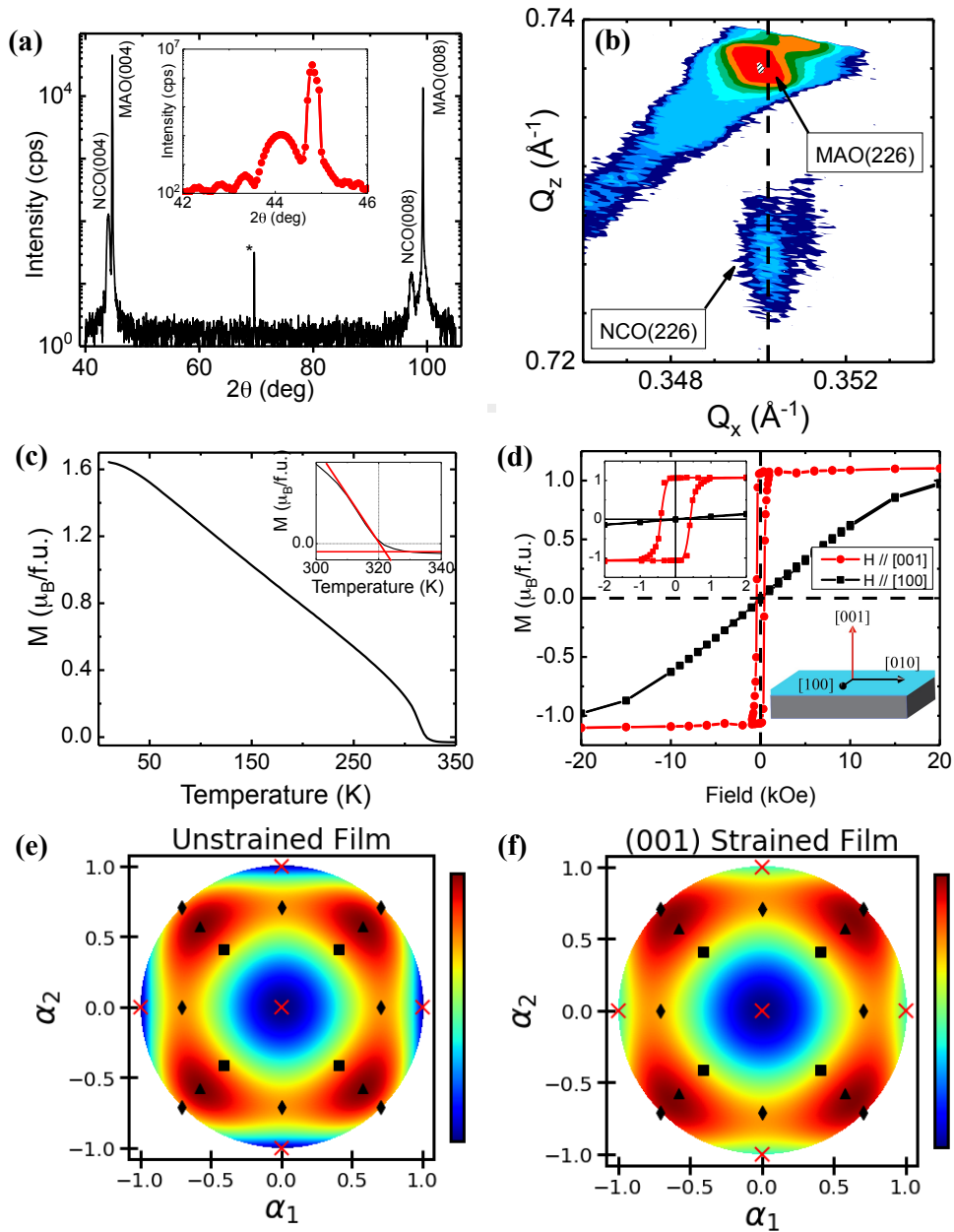


Figure 2. Structural and magnetic behavior of (001)-oriented films. (a) θ - 2θ scan of NCO/MAO(001). Inset is a scan of the NCO (004) peak. (b) Reciprocal space mapping of (226) peaks of NCO and MAO. Alignment of peaks along the Q_x axis indicates in-plane lattice matching of the film to the MAO substrate. (c) M - T curve of NCO/MAO(001) film field-cooled in a 100 Oe out-of-plane magnetic field. The inset shows the upturn of magnetization occurring at $T_C = 323$ K. (d) M - H relations at 150 K. The upper-left inset shows magnetization behavior closer to the origin. Lower-right inset shows a sketch of the sample. The magnetic anisotropy energy $F(\alpha_1, \alpha_2)$ of a cubic material without strain (e), and with a compressive biaxial strain in the (001) plane (f), is calculated from the Landau theory. The cross, diamond, square, and triangle symbols indicate [100], [110], [11-2], [111] directions or their cubic equivalent, respectively. The calculation uses the experimentally-determined values of constants $B_1/K_1 = -11.96$ and $B_2/K_1 = -18.45$.

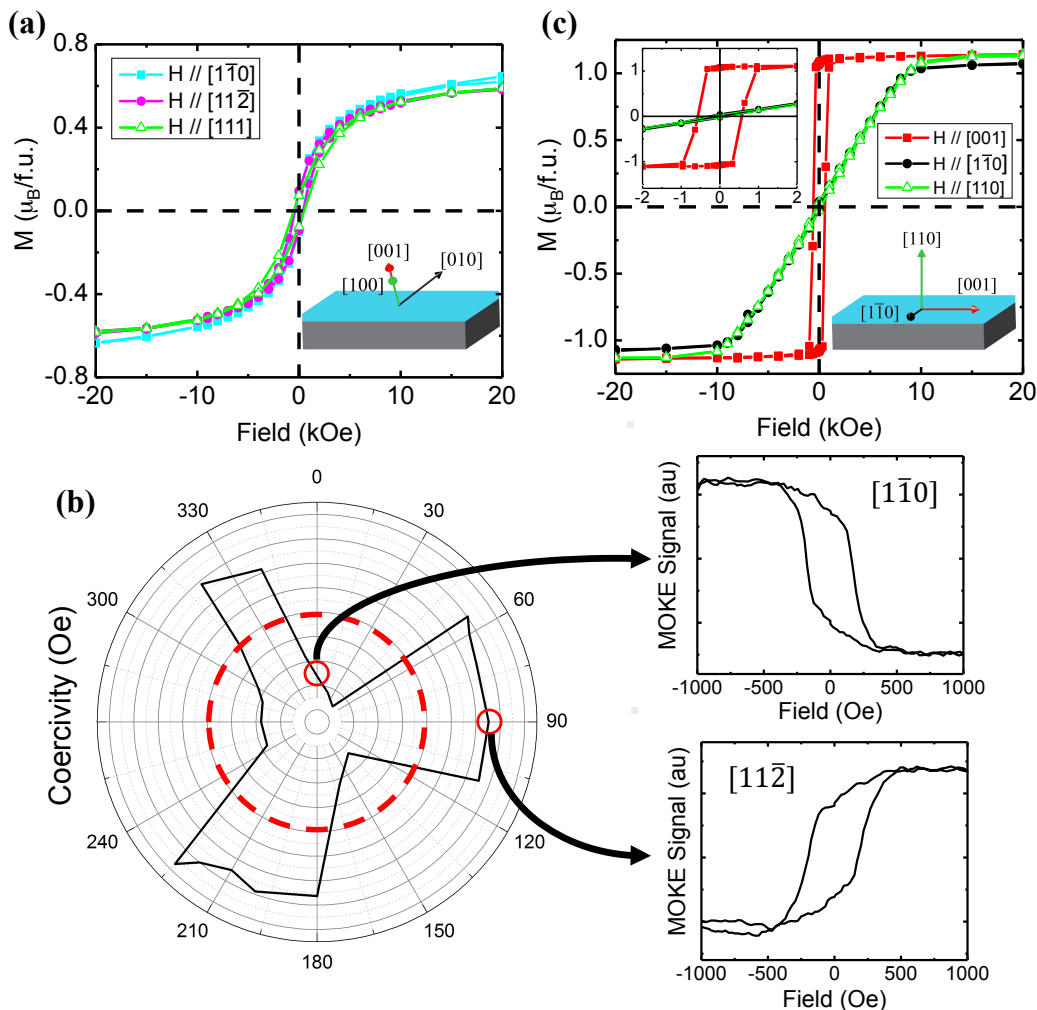


Figure 3. Magnetic behavior of (111)- and (110)-oriented NCO films. (a) M - H relation along the out-of-plane and two in-plane directions of the (111)-oriented films measure at 150 K. Inset is a schematic of the (111)-oriented film. **(b)** Polar plot of the coercivities of the hysteresis loops measured using MOKE at room temperature (see text). The red dashed circle indicates zero coercivity; i.e. values outside the circle have a hysteresis loop with positive saturation at high fields (“normal”), while values inside the circle have a hysteresis loop with positive saturation at negative fields (“inverted”). Examples of each type of loop are shown at the angles. The corresponding crystallographic direction along which the magnetic field is applied is shown on the individual plots. **(c)** M - H relation at 150 K for the (110)-oriented films. Upper-left inset further shows magnetization behavior closer to the origin. Lower-right inset shows a sketch of the sample with axes labeled.

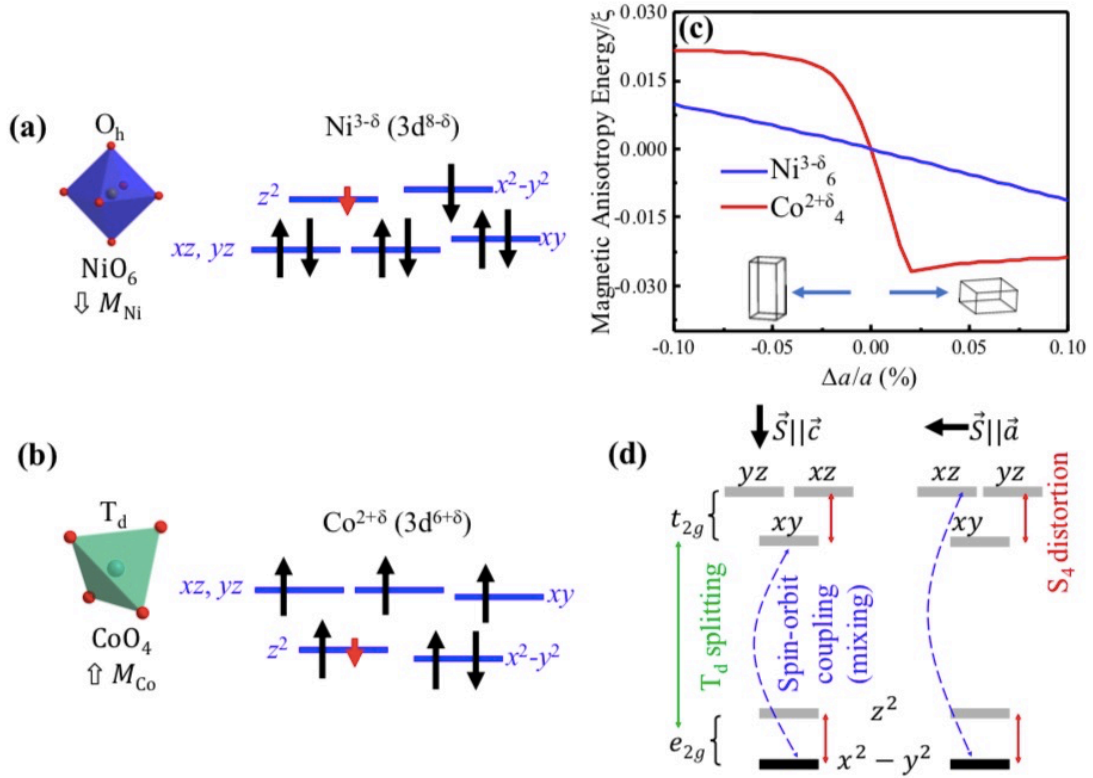


Figure 4. Microscopic model of the effect of the biaxial strain in the (001) plane. (a)-(b) Octahedral and tetrahedral environments of magnetic nickel and cobalt sites, respectively. The energy diagrams show the splitting between e_g and t_{2g} levels, as well as the smaller splitting within the symmetry groups due to the tetragonal strain distortions. The short arrows represent partial (δ) occupation of the orbital. **(c)** The magnetic anisotropy energy calculated from the single-ion magnetic anisotropy as a function of in-plane biaxial strain, where $\xi = 50$ meV is the spin-orbit coupling constant; the magnitude of V_{CF} and E_x are set as 1 eV and 5 eV respectively. **(d)** Relative energies of mixing states due to the spin-orbit coupling. The energy gain is larger when the spin is along the c axis than that when the spin is perpendicular to the c axis, leading to magnetocrystalline anisotropy.

Table I. Magnetic anisotropy and magnetoelastic coupling coefficient of NiCo₂O₄ measured in this work.

K_u (MJ/m ³)	K_1 (MJ/m ³)	B_1 (MJ/m ³)	B_2 (MJ/m ³)
0.23 (20 K)	0.54 (150 K)	-14.1 (20 K)	-10 (150 K)
0.1 (150 K)	0.08 (300 K)	-6.5 (150 K)	-1.5 (300 K)
0.02 (300 K)		-1.1 (300 K)	

Supplementary Information

Perpendicular Magnetic Anisotropy in Conducting NiCo₂O₄ Films from Spin-Lattice Coupling

Corbyn Mellinger¹, Jace Waybright^{1,2}, Xiaozhe Zhang^{1,3}, Caleb Schmidt¹, and Xiaoshan Xu^{1,4}

¹ Department of Physics and Astronomy, University of Nebraska, Lincoln, Nebraska 68588, USA

² Department of Physics, South Dakota State University, Brookings, SD 57007 USA

³ School of Materials Science and Engineering, Xi'an Polytechnic University, Xi'an, 710048, China

⁴ Nebraska Center for Materials and Nanoscience, University of Nebraska, Lincoln, Nebraska 68588, USA

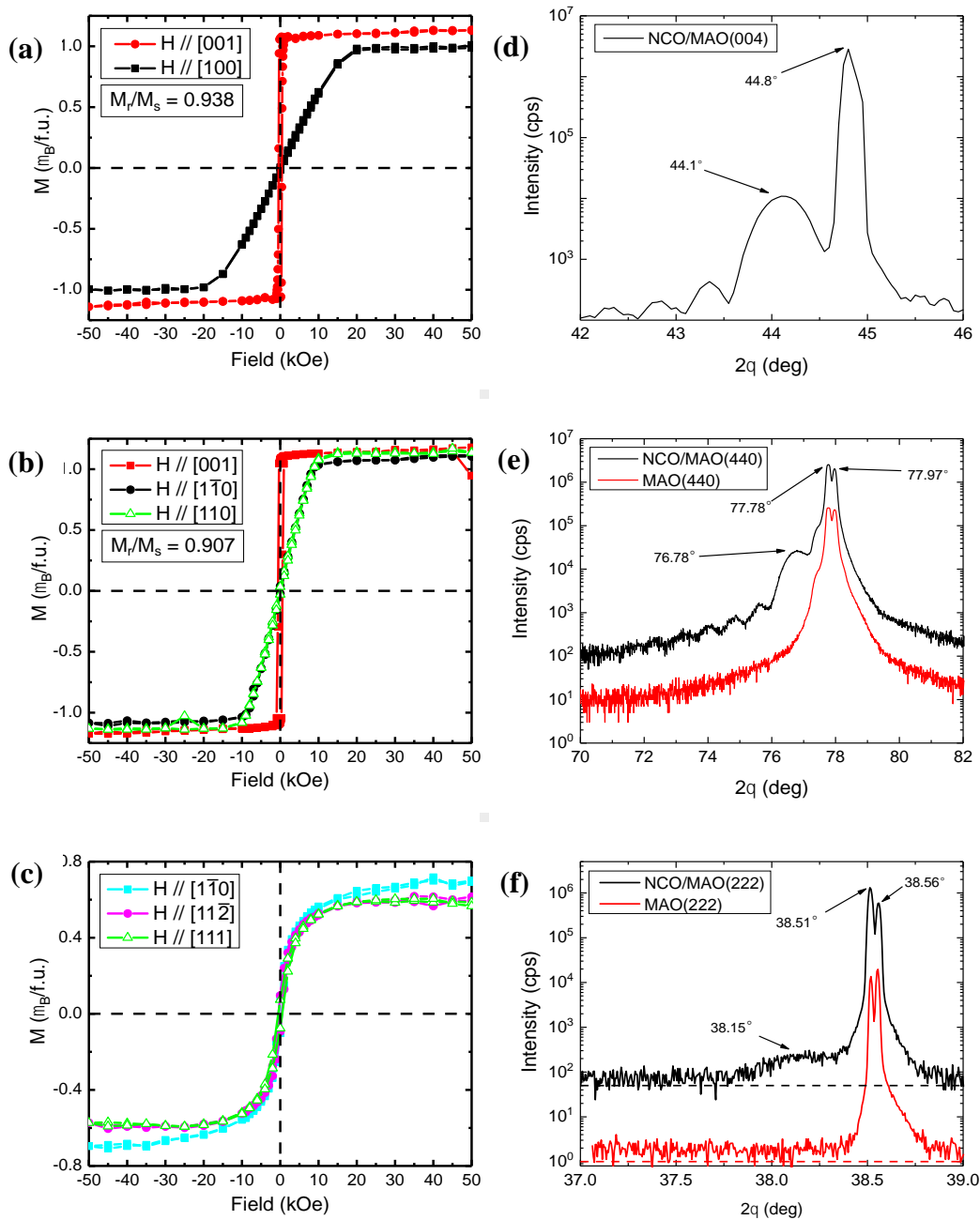
S1. SQUID & XRD Supplementary

An expanded view of the M-H curves from the main text (Figs. 2(b), 3(a), 3(c)) is given in Figure S1(a)-(c). Applied field of up to 50 kOe confirm the films have reached their full saturation magnetizations. Interestingly, the (001) oriented film in Fig. S1(a) has differing saturation magnetizations for the out-of-plane [001] and in-plane [100] directions. This phenomenon has been seen in cobalt ferrite thin films, and can be attributed to the coupling of the orbital angular momentum with the spin-orbit interaction, which arise due to the strain-induced recombination of d-orbitals [1].

S2. MOKE Supplementary

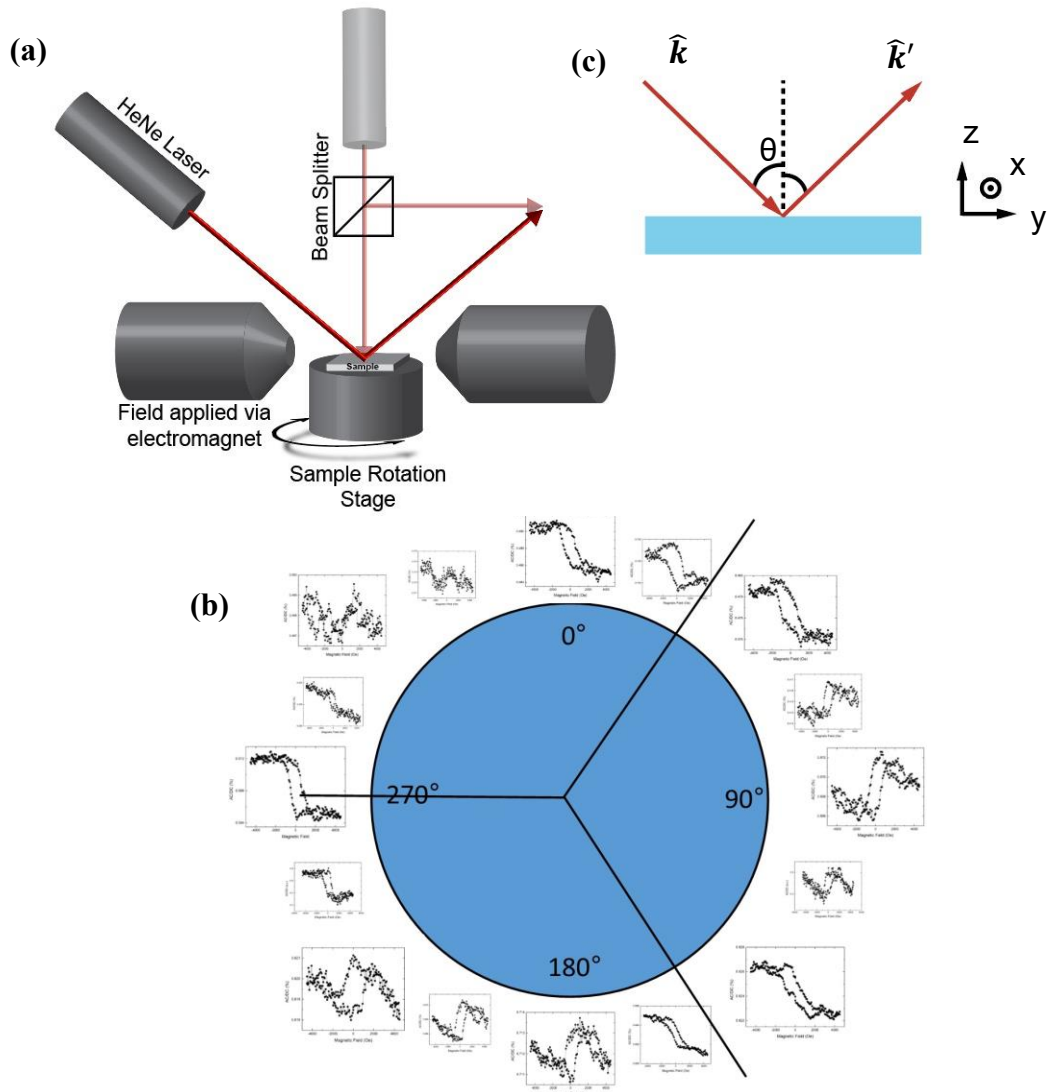
Magneto-optical Kerr Effect (MOKE) measurements on the NCO/MAO(111) structures are made at room temperature using an experimental configuration as outlined in Sato [2]. An intensity-stabilized HeNe laser ($\lambda = 632$ nm) is used as the probing laser. The first polarizer generates the s-polarization of light for interaction with the sample. Magnetic fields of up to 5 kOe are generated using an electromagnet. Additionally, the samples are mounted on an Aluminum stand, which is attached to a goniometer with markings every 1°. The surface of the Al stand was machined to be flat, to avoid tilting of the sample during rotation. In the longitudinal MOKE geometry, the magnetic field is applied in the plane of the sample, and the polarized laser incident at $\sim 30^\circ$ from the sample normal. A diagram of the sample holder is shown in Figure S2(a). A field sweep at a fixed angle is done several times and averaged to reduce noise. The goniometer is then rotated, and the field sweeps are repeating, giving hysteresis loops at several angles. Importantly, since the magnetic field is not rotated along with the sample, the crystallographic direction along which the field is applied changes, and the measurement looks at the magnetization along that direction, allowing for in-plane magnetic anisotropy of the sample to be studied. Through the rotation, hysteresis loops would change from so-called “regular” loops (in which application of a positive saturation field brings the Kerr rotation to its maximum) to so-called “inverted” loops (in which application of a positive saturation field brings Kerr rotation to its minimum). We analyze these loops using the coercivity, denoting the “regular” loops with coercivity positive and equal to its magnitude, and “inverted” loops with coercivity negative and equal to its magnitude. Raw data from the angular-dependent hysteresis loops are show in Figure S2(b), with the lines drawn to highlight the three-fold symmetry seen. These graphs correspond to the coercivities used in Figure 3(b).

Our observation of angle-dependent hysteresis leads directly from the strong anisotropy of the NCO along the (001) axes. Typical explanations of Kerr effect measurements assume sample magnetization aligning with the external field, but this is not necessarily the case. This can be seen by considering a 3-dimensional Stoner-Wohlfarth model of magnetic domains, in which the magnetic energy has terms from anisotropy



51 **Figure S1** | (a)-(c): Expansion of SQUID figures from Figs. 2(a)-(b), 3(a) to 50 kOe. (d)-(f): Out-of-plane diffraction
 52 data for the three orientations of film studied. 2θ values of the peaks are labeled for clarity. Double-peaks appear for
 53 the substrate due to the presence of significant $Cu-K\alpha_2$ in addition to $Cu-K\alpha_1$. The determination of out-of-plane strain
 54 for the three sample orientations were determined using $\theta-2\theta$ XRD on the Rigaku SmartLab, and the plots are given
 55 in (d)-(f), with (e) and (f) also showing the diffraction of patterns of the substrates alone. All x-ray data uses $Cu-K\alpha$
 56 wavelengths from a Rigaku SmartLab system.

57
 58
 59



60
61
62
63
64
65
66
67
68
69
70
71
72
73
74
75
76
77

Figure S2 | (a) Diagram of the relative positions of sample, rotation stage, electromagnet, and laser used in longitudinal MOKE measurements. Transparent portion of the figure is the configuration used when measuring polar MOKE using in-plane magnetic field, a so-called “hybrid MOKE” configuration. Since the magnetization lies largely out-of-plane, this measurement provides non-zero Kerr rotation. (b) Example of raw data from a longitudinal MOKE measurement as a function of rotation angle. Data is more noisy at points where the magnetization is much lower along the plane of reflection. (c) Diagram of the geometry used in the Lorentz force derivation just above.

78
79
80
81
82
83
84
85
86
87
88
89
90
91
92
93
94
95
96
97
98
99
100
101
102
103
104
105
106
107
108
109
110
111
112
113
114
115
116
117
118
119
120
121
122
123
124
125
126

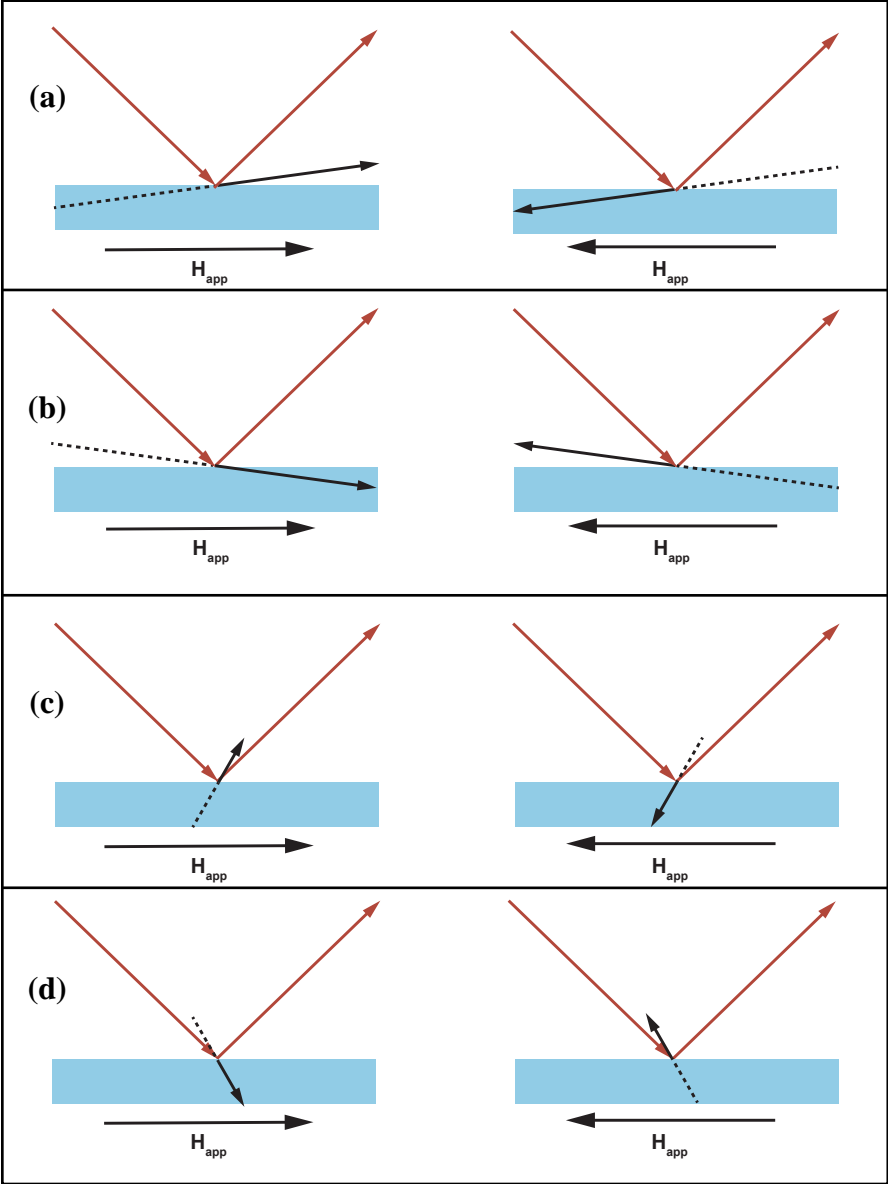


Figure S3 | Visualization of the MOKE measurement under several relative orientations of \hat{k}' , \hat{m} . In both (a) and (b), the magnetization lies nearly in-plane. In (a), $\hat{k}' \cdot \hat{m} > 0$ for \vec{H} pointing right, and < 0 when pointing left. (b) shows the same sample and magnetization orientation, but rotated by 180° . In this case, again, $\hat{k}' \cdot \hat{m} > 0$ for field pointing right, and < 0 for field pointing left. By contrast, (c) and (d) have a magnetization lying much closer to perpendicular to the sample surface. In (c), $\hat{k}' \cdot \hat{m} > 0$ for applied field pointing right, and < 0 for field pointing left. However, once the sample is rotated by 180° as shown in (d), $\hat{k}' \cdot \hat{m} < 0$ for field pointing right, and > 0 for field pointing left. The signs of the Kerr rotation have not changed between (a) and (b), while the signs of the Kerr rotation have changed between (c) and (d). These latter two figures apply to the highly out-of-plane easy axes for the NCO/MAO (111) structure, leading to the flipping of hysteresis loops as the sample is rotated.

127 and Zeeman contributions: $E = K \sin^2(\alpha) - HM \sin(\theta) \cos(\phi) = K \left[\sin^2(\alpha) - \frac{HM}{K} \sin(\theta) \cos(\phi) \right]$, with
 128 θ, ϕ the spherical angles of magnetization, and α the angle between magnetization and anisotropy axis. As
 129 the anisotropy scale K increases, the magnetization direction of minimum energy tilts further from the field
 130 direction and more towards the anisotropy axis.

131
 132 A consequence of the relative orientations of the laser incidence and magnetization is that a large enough
 133 misalignment of the directions leads to a flipping of the sign of the magneto-optic effect. Explicitly,
 134 $\hat{k}' \cdot \hat{m} = 0$ when the angle of incidence satisfies $\tan(\theta) = \frac{m_z}{m_y}$, and on either side of this value, the effect of
 135 the magnetization switches signs. This is displayed visually in the supplementary Fig S3(a)-(d). The severe
 136 misalignment of the laser k' -vector and magnetization direction seen in the NCO/MAO(111) measurements
 137 leads directly to the emergence of inverted hysteresis loops, and the three-fold rotational symmetry of the
 138 angle-dependent MOKE measurement.

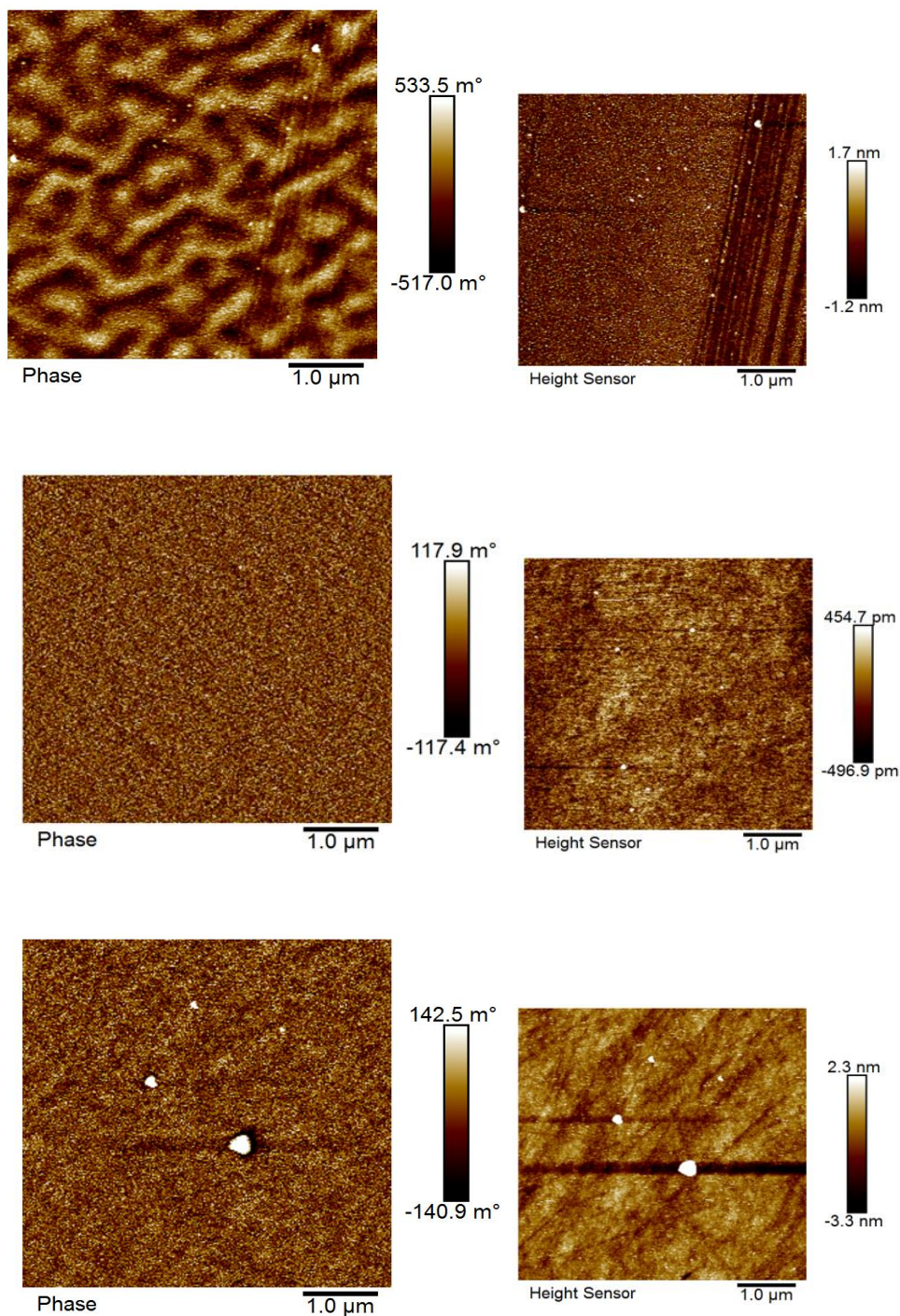
139
 140 We can further analyze the effect of magnetization direction relative to incidence direction modeling the
 141 Magneto-optic Kerr Effect in terms of the Lorentz force experienced by charges in the magnetized
 142 material. In our case of s-polarized light (i.e. polarization perpendicular to the plane of reflection), the
 143 electric field forces an oscillation of the charges, which then experience a Lorentz force. With light
 144 polarization along the x-axis (i.e. s-polarized light), charges will be forced to oscillate along this same
 145 axis. Given the most general magnetization direction $\hat{m} = (m_x, m_y, m_z)$, the force experienced will be
 146 $\hat{F} \sim \hat{x} \times (m_x \hat{x} + m_y \hat{y} + m_z \hat{z}) = m_y \hat{z} - m_z \hat{y}$. The induced p-polarization is what will be measured, and
 147 the axis of the p-polarization lies within the plane of reflection, and perpendicular to the direction of
 148 reflected light. For a general direction of incident light $\hat{k} = \sin(\theta) \hat{y} - \cos(\theta) \hat{z}$, as illustrated in Figure
 149 S3(c), the reflected light will follow $\hat{k}' = \sin(\theta) \hat{y} + \cos(\theta) \hat{z}$. The rotated polarization will have
 150 component along the p-polarization direction, which can be represented as $\hat{p} = -\cos(\theta) \hat{y} + \sin(\theta) \hat{z}$.
 151 The measured Kerr rotation will be proportional to the amount of new polarization lying in this plane, or
 152 $\hat{F} \cdot \hat{p} = m_z \cos(\theta) + m_y \sin(\theta) = \hat{k}' \cdot \hat{m}$. Repeating calculations for the case of p-polarized light yields
 153 the similar result that the Lorentz force induces rotation proportional to $\hat{k} \cdot \hat{m}$.

154
 155

156 **S3. Magnetic Force Microscopy**

157
 158 Direct imaging of the domain structure of NCO on MAO (001), (110), and (111) substrates is performed
 159 using magnetic force microscopy (MFM) in a Bruker ScanAsyst system, with a commercially available
 160 magnetic tip. A bar magnet with a strength of ~ 400 Oe was used to pole the sample before scanning. With
 161 the magnetic tip normal to the sample, magnetization pointing normal to the surface is sensitive to scanning,
 162 while in-plane magnetization is undetectable. Thus, the MFM provides a confirmation of easy of out-of-
 163 plane versus in-plane magnetization. To differentiate the magnetic effects of tip deflection from
 164 topographical features, an additional scan using AFM is done in the area of interest, and the AFM
 165 component is removed from the total scan signal. Typical MFM and AFM scans of (001), (110), and (111)
 166 oriented samples are shown in Figs. S4 (a)-(f). No domains are seen in the (110) and (111) samples, while
 167 domains of ~ 500 nm are seen in (001) samples, demonstrating magnetization out-of-plane for this
 168 orientation.

169
 170
 171
 172
 173
 174



175 **Figure S4 | Magnetic force microscopy and atomic force microscopy data for the three NCO orientations**
 176 **studied. (a):** NCO/MAO (001) MFM; **(b):** NCO/MAO (110) MFM; **(c):** NCO/MAO (111) MFM. **(d)-(f)** are the AFM
 177 images taken over the regions shown in **(a)-(c)**, respectively. Only **(a)** shows considerable magnetic behavior in the
 178 out-of-plane direction measured, which is consistent with the measurements by SQUID showing only the (001)-
 179 oriented NCO having easy magnetization out-of-plane.

180
 181
 182

S4. Landau Theory of Spin-Lattice Coupling

The full magnetic cubic anisotropy energy and magnetoelastic energy is given as:

$$F = K_1(\alpha_1^2\alpha_2^2 + \alpha_2^2\alpha_3^2 + \alpha_3^2\alpha_1^2) + B_1(\alpha_1^2e_{xx} + \alpha_2^2e_{yy} + \alpha_3^2e_{zz}) + B_2(\alpha_1\alpha_2e_{xy} + \alpha_2\alpha_3e_{yz} + \alpha_3\alpha_1e_{zx}),$$

with terms as described in the main text. Explicitly in the case of strained (001) films, the compressive normal stress on the cubic faces of the unit cell makes off-diagonal shear strain terms zero, with $e_{xx}, e_{yy} < 0$ and $e_{zz} > 0$. Compressive strain in the (001) plane means $e_{xx} = e_{yy} \equiv e_{in}$; $e_{zz} = e_{out}$, where e_{in} and e_{out} are the in-plane and out-of-plane strains. In all cases, $e_{in} = -0.003$ from the lattice mismatch and the observation that films are epitaxially strained to the substrate (Figure 1(b) in the main text). The value of e_{out} is determined experimentally from θ - 2θ measurements shown in Figure S1(d)-(f). Additionally, the squares of directional cosines sum to unity so that α_3 can be expressed in terms of α_1, α_2 . Applying these simplifications:

$F = K_1(\alpha_1^2 + \alpha_2^2 - \alpha_1^4 - \alpha_2^4 - \alpha_1^2\alpha_2^2) + B_1(e_{in} - e_{out})(\alpha_1^2 + \alpha_2^2) + B_1e_{out}$. First derivatives with respect to α_1, α_2 are taken and set to zero to find potential critical values of energy, and the sign of second derivatives with respect to α_1, α_2 show the possible magnetization directions to be maxima, minima, or saddle points in energy. For the (001) samples, the procedure gives solutions summarized below in Table S1.

Table S1: Solutions to free-energy minimization of strained (001)-oriented NCO. $\langle 110 \rangle$ and $\langle 111 \rangle$ directions remain difficult to magnetize regardless of relation between K_1, B_1 . $\Delta e \equiv e_{in} - e_{out}$.

#	α_1	α_2	$\frac{\partial^2 F}{\partial \alpha_1^2}$	$\frac{\partial^2 F}{\partial \alpha_2^2}$	Axis	$\frac{K_1}{+ \Delta e B_1} > 0$	$\frac{K_1}{+ \Delta e B_1} < 0$
1	0	0	$2K_1 + 2\Delta e B_1$	$2K_1 + 2\Delta e B_1$	$[0, 0, \pm 1]$	Easy	Hard
2	0	$\pm \sqrt{\frac{K_1 + \Delta e B_1}{2K_1}}$	$K_1 + \Delta e B_1$	$-4(K_1 + \Delta e B_1)$	$[0, \pm 1, \pm 1 + \delta]$	Saddle	Saddle
3	$\pm \sqrt{\frac{K_1 + \Delta e B_1}{2K_1}}$	0	$-4(K_1 + \Delta e B_1)$	$K_1 + \Delta e B_1$	$[\pm 1, 0, \pm 1 + \delta]$	Saddle	Saddle
4	$\pm \sqrt{\frac{K_1 + \Delta e B_1}{3K_1}}$	$\pm \sqrt{\frac{K_1 + \Delta e B_1}{3K_1}}$	$-\frac{8(K_1 + \Delta e B_1)}{3}$	$-\frac{8(K_1 + \Delta e B_1)}{3}$	$[\pm 1, \pm 1, \pm 1 + \delta]$	Hard	Easy

For example, Solution #4 has $\alpha_1^2 = \alpha_2^2$ so the axis will lie in $(\pm 1, \pm 1, 0)$ plane. Since $\Delta e B_1$ is small, α_3^2 will be very close to $\frac{1}{3}$ (and thus the to the $\langle 111 \rangle$ axes), but will in general differ, giving the small rotation, denoted generally by δ in Table S1.

Anisotropy energy can be directly measured from hysteresis curves, which then provides values of anisotropy and magnetoelastic constants. The (001) samples were measured with magnetization along $[100]$ and $[001]$, as shown in Fig. 2(a), which have magnetic energies $e_{in}B_1$ and $e_{out}B_1$, respectively. In other words, the cubic magnetic anisotropy is broken, with $[100]$ and $[010]$ axes raising in energy and $[001]$ axis lowering.

The (111) NCO experiences only shear strains, with stresses along the body diagonals of the unit cell, in other words, the strain tensor satisfies $e_{ii} = 0$; $e_{ij} = e > 0$. The magnetic energy involves only K_1 and B_2 constants: $F_{(111)} = K_1(\alpha_1^2\alpha_2^2 + \alpha_2^2\alpha_3^2 + \alpha_3^2\alpha_1^2) - e_{in}B_2(\alpha_1\alpha_2 + \alpha_2\alpha_3 + \alpha_3\alpha_1)$. Magnetic energies are tabulated in Table S3.

219 (110) oriented NCO has a combination of both shear and normal strains, which means $K_1, B_1,$ and B_2 terms
 220 are all included in the magnetic energy expression. Explicitly written in terms of e_{out} and e_{in} :
 221 $F_{(110)} = K_1(\alpha_1^2\alpha_2^2 + \alpha_2^2\alpha_3^2 + \alpha_3^2\alpha_1^2) + B_1\left(\frac{e_{out}+e_{in}}{2}\right)(\alpha_1^2 + \alpha_2^2) + e_{in}B_1\alpha_3^2 + B_2\left(\frac{e_{out}-e_{in}}{2}\right)\alpha_1\alpha_2.$
 222 Energies along measured directions are listed in Table S4.
 223

224 **Table S2: Summary of magnetization energetics along measured directions for the (001)-oriented**
 225 **NCO in strained and unstrained cases.**

Mag. Direction	F(unstrained)	F(strained)	$F_{(001)}^{[100]} - F_{(001)}^{[001]}$
[001]	0	$e_{out}B_1$	$(e_{in} - e_{out})B_1$
[100]	0	$e_{in}B_1$	

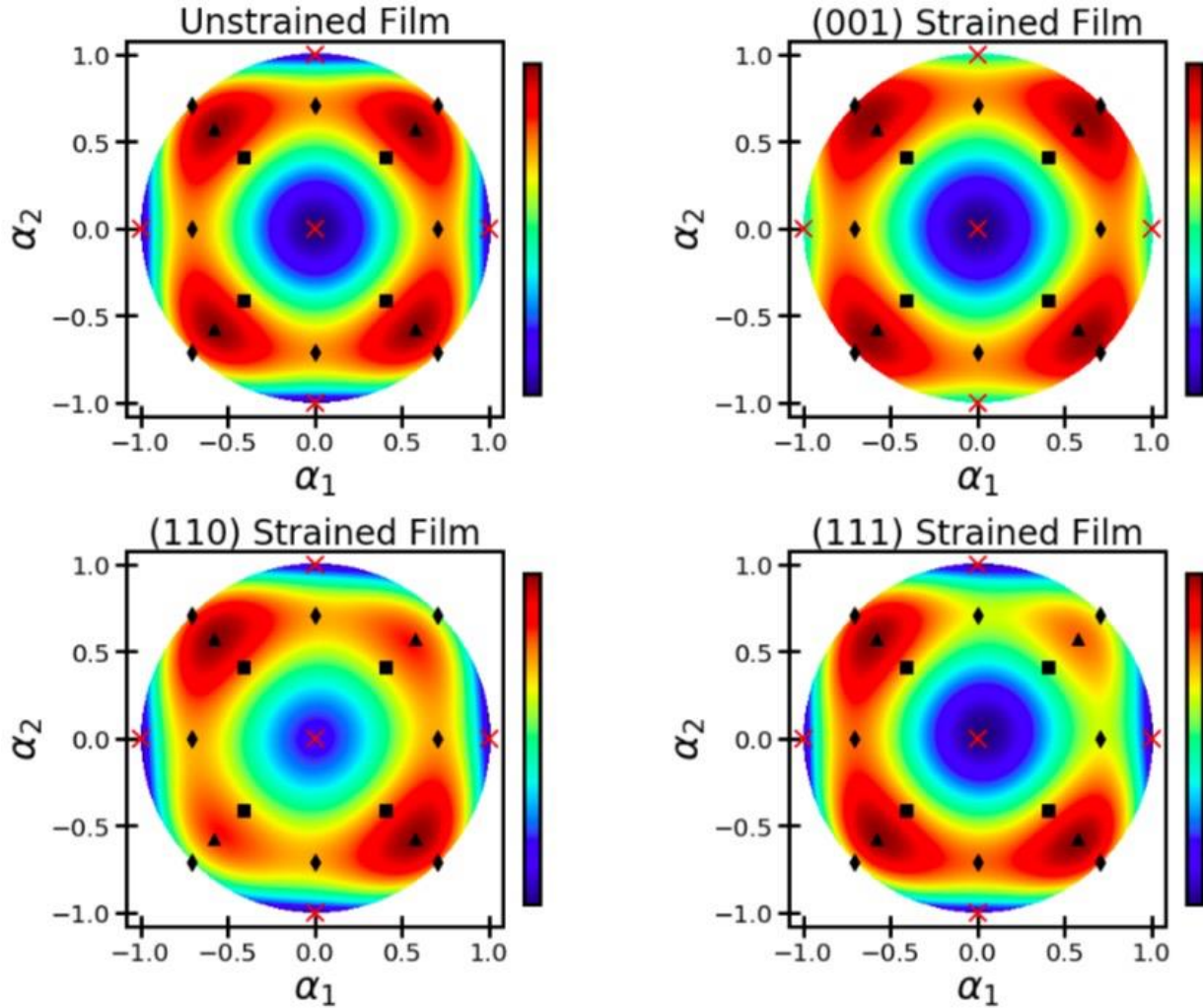
226
 227 **Table S3: Summary of magnetization energetics along measured directions for the (111)-oriented**
 228 **NCO in strained and unstrained cases.**

Mag. Direction	F(unstrained)	F(strained)	$F_{(111)}^{[111]} - F_{(111)}^{[11\bar{2}]}$
[111]	$\frac{K_1}{3}$	$\frac{K_1}{3} - e_{in}B_2$	$\frac{K_1}{12} - \frac{3e_{in}B_2}{2}$
[11 $\bar{2}$]	$\frac{K_1}{4}$	$\frac{K_1}{4} + \frac{e_{in}B_2}{2}$	
[1 $\bar{1}$ 0]	$\frac{K_1}{4}$	$\frac{K_1}{4} + \frac{e_{in}B_2}{2}$	—

229
 230 **Table S4: Summary of magnetization energetics along measured directions for the (110)-oriented**
 231 **NCO in strained and unstrained cases.**

Mag. Direction	F(unstrained)	F(strained)	$F_{(110)}^{[1\bar{1}0]} - F_{(110)}^{[110]}$
[001]	0	$e_{in}B_1$	—
[110]	$\frac{K_1}{4}$	$\frac{K_1}{4} + B_1\left(\frac{e_{out} + e_{in}}{2}\right) - \frac{B_2}{2}\left(\frac{e_{out} - e_{in}}{2}\right)$	$B_2\left(\frac{e_{out} - e_{in}}{2}\right)$
[1 $\bar{1}$ 0]	$\frac{K_1}{4}$	$\frac{K_1}{4} + B_1\left(\frac{e_{out} + e_{in}}{2}\right) + \frac{B_2}{2}\left(\frac{e_{out} - e_{in}}{2}\right)$	

232
 233
 234 With all 3 orientations of NCO, the constants K_1, B_1, B_2 can be determined experimentally. From Tables
 235 S2-S4, we see that (001) M - H curves can uniquely determine the value of B_1 , that B_2 can be determined
 236 based on (110) M - H curves, and that the (111) M - H curves can determine the relation between B_2 and K_1 ,
 237 and thus give K_1 . In the special observed case that $F_{(111)}^{[111]} - F_{(111)}^{[11\bar{2}]} = 0$, the relation between K_1 and B_2 is
 238 $K_1 = 18e_{in}B_2$. The anisotropy energy is directly measurable from the hysteresis curves, using the
 239 saturation magnetization and field required to reach saturation: $U = \frac{1}{2}\mu_0 M_s H_A$. Given these relations, we
 240 can find the magnetization energy constants which are listed in Table I of the main text:
 241 $K_1 = 5.4 \times 10^5 \frac{J}{m^3}, B_1 = -6.5 \times 10^6 \frac{J}{m^3}, B_2 = -1.0 \times 10^7 \frac{J}{m^3}.$
 242



243
 244
 245
 246
 247
 248
 249
 250
 251
 252
 253
 254
 255
 256
 257
 258
 259
 260
 261
 262

Figure S5 | Summary of magnetization energies from Landau theory considerations. (a): Unstrained cubic magnetic anisotropy. The [001], [100], and [010] magnetization directions are degenerate global minima of magnetization energy. (b): Cubic material under biaxial strain in (001) plane. The [001] axis has lowered relative to the other edge directions, giving the out-of-plane anisotropy. Panes (a), (b) are exactly the same as those in Fig. 2(c) and (d), respectively. (c): Magnetic energy of cubic material under biaxial strain in (110) plane. The [001] axis remains as a global minimum, but the true magnetization energy minima lie along [100], [010] axes. (d): Magnetic energy of cubic material under biaxial strain in (111) plane. The magnetization energy degeneracy along the $\langle 111 \rangle$ axes is broken, with the true out-of-plane [111] direction easier to magnetize than others in that class. As in Figure 2, the cross, diamond, square, and triangle markers indicate the $\langle 001 \rangle$, $\langle 110 \rangle$, $\langle 11\bar{2} \rangle$, and $\langle 111 \rangle$ crystal directions, respectively.

263 Relative energies can be determined for general magnetization direction by plotting the magnetic free
 264 energy as a function of magnetization directions α_1, α_2 with experimentally-determined strain and
 265 anisotropy energy values used as given in Table I. The unstrained plot in Fig. S5(a) shows the cubic
 266 anisotropy, i.e. lower energies along [001] ($\alpha_1 = \alpha_2 = 0$), [100] ($\alpha_1 = 1, \alpha_2 = 0$), and [010] ($\alpha_1 = 0, \alpha_2 =$
 267 1) axes. Energy landscape for the three orientations of strained films are shown, using strain values as
 268 determined by θ -2 θ x-ray diffraction [Figs. S1 (d)-(f)]. RSM of the (001)-oriented film at the (226) film
 269 plane [Fig. 1(b)] confirms in-plane lattice matching, so pinned strains of -0.3% are assumed for all in-plane
 270 directions, with out-of-plane strains determined by x-ray diffraction. For ease of determination of common
 271 axis directions, the diamonds are $\langle 110 \rangle_c$ axes, triangles are $\langle 111 \rangle_c$ axes, squares are $\langle 11\bar{2} \rangle_c$ axes, and red
 272 crosses are $\langle 001 \rangle_c$ axes.

273
 274 The true easy magnetization direction for the strained (110) film was not measured in our study; the true
 275 easy axes [100] and [010] lie neither exactly in-plane or out-of-plane of the sample. The strain is not
 276 sufficient to bring the [001] axis out of a local minimum, so it appears relatively easy. Considering that the
 277 other two axes measured are [110] and [1-10], the in-plane [001] axis is the easiest measured.

278
 279 In the case of the (111) strained film, the $\langle 001 \rangle$ axes remain the global minima, but some deviation from
 280 this direction is noticeable; the dark blue minimum along [001] shifts slightly towards the [111] direction.
 281 Additionally, the [111] axis is lower in energy than the [-111], [1-11], and [11-1] axes. It is clear that the
 282 effect of the strain is to make the out-of-plane direction easier or harder to magnetize.

283
 284

285 S5. Microscopic Mechanism of Spin-lattice Coupling

286
 287 Modeling the octahedral and tetrahedral environments of Ni and Co atoms is done by considering the
 288 Hamiltonian involving the free energy of the electron, electric field generated by the negatively-charged
 289 oxygen sites, spin-orbit coupling, and exchange interaction, explicitly written as
 290 $H = \sum_i \left[\frac{p_i^2}{2m} - \frac{Ze}{4\pi\epsilon_0 r_i} + V_{CF} + \xi \vec{S}_i \cdot \vec{l}_i + E_x \vec{S}_i \cdot \hat{B}_{ex} \right]$. The Hamiltonian is then diagonalized, and
 291 eigenstates corresponding to the $d_{x^2-y^2}, d_{z^2}, d_{xy}, d_{yz}, d_{xz}$ orbitals are obtained, and their eigen-energies
 292 determined. These yield splitting of e_g and t_{2g} symmetry's energies as determined from classical crystal
 293 field theory. Then, perturbations of the octahedra and tetrahedra are analyzed using perturbation theory,
 294 and their energy levels determined. As an illustration of the physics involved, one such example is done
 295 analytically in the following sections, but full analysis is performed using numerical methods and plotting
 296 using open-access pycsi and matplotlib packages.

297
 298
 299 I: Crystal-field, Structural distortion, Exchange field components

300
 301 Real wavefunctions $d_{x^2-y^2}, d_{z^2}$, etc. are linear combinations of the spin-orbit basis, and the separation
 302 between higher-energy e_g states (in the octahedral environment) represented by an additional energy term
 303 D, with $D \sim$ exchange splitting energy.

304
 305 The crystal field energy consists of Coulomb interaction between electrons and the charged oxygen ligands.
 306 Since the energy scale is relatively small in comparison with the ionic interactions, the energy can be expand
 307 in terms of Legendre polynomials, using the notation of Arfken (7th ed., pg. 737):
 308

309
$$V_{CF}(\vec{r}) = \sum_i^N \frac{Ze^2}{4\pi\epsilon|\vec{R}_i - \vec{r}|} = \frac{Ze^2}{4\pi\epsilon} \sum_i \sum_{k=0}^{\infty} \frac{1}{r_{>}} \left(\frac{r_{<}}{r_{>}}\right)^k P_k(\cos(\omega_i))$$

310 with $r_{<}, r_{>}$ being the smaller and larger of \vec{R}_i and \vec{r} , Z being the charge of the N ligands, and i running over
 311 the positions of the crystal field ligands. The Legendre polynomials may be expanded in terms of the
 312 spherical harmonics:

313
$$P_k(\cos(\omega_i)) = \frac{4\pi}{2k+1} \sum_{m=-k}^k Y_{km}(\theta, \phi) Y_{km}^*(\theta_i, \phi_i)$$

314 ,where (R_i, θ_i, ϕ_i) and (r, θ, ϕ) are the spherical coordinates of the ligands and of the electron, respectively.
 315 Within the localized single-electron treatment, we can safely replace $r_{<}$ with r and $r_{>}$ with R_i , giving an
 316 energy term with the form
 317
 318

319
$$V_{CF} = \frac{Ze^2}{4\pi\epsilon} \sum_i^N \sum_{k=0}^{\infty} \sum_{m=-k}^k \frac{1}{R_i} \left(\frac{r}{R_i}\right)^k \frac{4\pi}{2k+1} Y_{km}(\theta, \phi) Y_{km}^*(\theta_i, \phi_i)$$

320 For a general configuration of crystal field ligands. In the case of the O_h symmetry, all $|R_i| = R$, we recast
 321 the equation in a simpler form:
 322

323
$$V_{CF}(\vec{r}) = \frac{Ze^2}{4\pi\epsilon R} \sum_{k=0}^{\infty} \sum_{m=-k}^k \left(\frac{r}{R}\right)^k \sqrt{\frac{4\pi}{2k+1}} \gamma_{km} Y_{km}(\theta, \phi)$$

324 ,where $\gamma_{km} \equiv \sqrt{\frac{4\pi}{2k+1}} \sum_{i=1}^N \left(\frac{R}{R_i}\right)^{k+1} Y_{km}^*(\theta_i, \phi_i)$, with R being the median distance from metal ion to oxygen
 325 ligand. The purpose of recasting the equation in this form will become apparent later in the derivation.
 326
 327

328 Matrix elements are populated using the inner product of V_{CF} with the spatial wavefunctions, which in terms
 329 of the separable hydrogen electron wavefunctions:
 330

331
$$V_{CF}^{m_1, m_2} = \iiint R_{n,l}^* Y_{l, m_1}^* V_{CF}(\vec{r}) R_{n,l} Y_{l, m_2} r^2 \sin(\theta) dr d\theta d\phi \quad (\text{S1})$$

332
 333
$$= \sum_{k=0}^{\infty} \sqrt{\frac{4\pi}{2k+1}} \gamma_{k, m_1 - m_2} U_{n,l,k} C^k(l, m_1, l, m_2)$$

334
 335 Where $U_{n,l,k} \equiv \frac{Ze^2}{4\pi\epsilon R^{k+1}} \int_0^{\infty} R_{nl}^2 r^{k+2} dr$, $C^k(l, m_1, l, m_2) \equiv \sqrt{\frac{4\pi}{2k+1}} \iint Y_{l, m_1}^* Y_{k, m_1 - m_2} Y_{l, m_2} \sin(\theta) d\theta d\phi$,
 336 the latter of which are known as the Gaunt coefficients and are related to the Clebsch-Gordan coefficients.
 337 Due to the rules of the CG coefficients, only k from 0 to $l_1 + l_2$ are nonzero, restricting the summation to
 338 a finite number of terms. Further, due to the symmetry of the O_h system, only even values of k will possibly
 339 contribute to the matrix element. In the case of the $l_1 = l_2 = 2$ for d-electrons this leaves only $k = \{0, 2, 4\}$.
 340 Additionally, by inspection one can verify that $\gamma_{2,0} = 0$ for the octahedral crystal field configuration.
 341

342 Finally, based on the octahedral symmetry in which the 6 oxygens have distance R and the angles of the 6
 343 ligands are $(\theta, \phi) = (0, 0), (\pi, 0), \left(\frac{\pi}{2}, \frac{\pi}{2}\right), \left(\frac{\pi}{2}, \frac{3\pi}{2}\right), \left(\frac{\pi}{2}, \pi\right), \left(\frac{\pi}{2}, 0\right)$, the sum over $N = 6$ reduces to:
 344

350
$$H_{CF} = U_{3,2,4} \begin{bmatrix} \gamma_{4,0} C_{-2,-2}^4 & 0 & 0 & 0 & \gamma_{4,4} C_{-2,2}^4 \\ 0 & \gamma_{4,0} C_{-1,-1}^4 & 0 & 0 & 0 \\ 0 & 0 & \gamma_{4,0} C_{0,0}^4 & 0 & 0 \\ 0 & 0 & 0 & \gamma_{4,0} C_{1,1}^4 & 0 \\ \gamma_{4,4} C_{2,-2}^4 & 0 & 0 & 0 & \gamma_{4,0} C_{2,2}^4 \end{bmatrix}$$

351
352
353
354
355
356
357
358
359
360
361
362
363

where $l_1 = l_2 = 2$ is suppressed from the Gaunt coefficients, which are now written C_{m_1, m_2}^k . Also note that $U_{n, l, k}$ provides an energy scale which may be factored out for the purpose of determining relative energy splittings, though some approximation may be made through the evaluation of the appropriate integral in its definition. Through calculation or a table of each coefficient, we get $C_{-2,-2}^4 = C_{2,2}^4 = \frac{1}{21}$, $C_{-1,-1}^4 =$

349 $C_{1,1}^4 = -\frac{4}{21}$, $C_{0,0}^4 = \frac{6}{21}$, $C_{-2,2}^4 = C_{2,-2}^4 = \frac{\sqrt{70}}{21}$, $\gamma_{4,4} = \gamma_{4,-4} = \sqrt{\frac{35}{8}}$, $\gamma_{4,0} = \frac{7}{2}$, and thus

352
353
$$H_{CF}^{(1)} = \frac{U_{3,2,4}}{6} \begin{bmatrix} 1 & 0 & 0 & 0 & 5 \\ 0 & -4 & 0 & 0 & 0 \\ 0 & 0 & 6 & 0 & 0 \\ 0 & 0 & 0 & -4 & 0 \\ 5 & 0 & 0 & 0 & 1 \end{bmatrix}$$

354
355
356
357
358
359
360
361
362
363

Diagonalization of this matrix to determine energy eigenvalues gives the splitting of e_g, t_{2g} symmetric levels.

The effect of compressive strain on the octahedron is to move oxygens in the xy -plane to distance $R - a$ from the metal ion, and move the polar oxygens to distance $R + c$ from the center, where a, c are small strains which are unrelated to the lattice constants of the crystal. In this case, $\gamma_{2,0} \neq 0$. Calculation gives

360 $\gamma_{2,0} = 2 \left\{ \left(1 - \frac{3c}{R}\right)^{-3} - \left(1 - \frac{3a}{R}\right)^{-3} \right\} \approx \frac{6(a-c)}{R}$. Changes to the $\gamma_{4,0}, \gamma_{4,4}$ terms are proportional to $\left(\frac{R}{R+a}\right)^5$

361 and $\left(\frac{R}{R+c}\right)^5$, and neglecting these higher order terms is warranted. Thus, the distortion introduces new terms

362 involving only $\gamma_{4,0}$ along the diagonal of the matrix. Explicitly:

364
$$H_{CF}^{(2)} = \frac{U_{3,2,2}}{7} \frac{6(a-c)}{R} \begin{bmatrix} -2 & 0 & 0 & 0 & 0 \\ 0 & 1 & 0 & 0 & 0 \\ 0 & 0 & 2 & 0 & 0 \\ 0 & 0 & 0 & 1 & 0 \\ 0 & 0 & 0 & 0 & -2 \end{bmatrix}$$

365
366
367

This interaction is spin-independent, so the full 10x10 matrices for the $|l_z, s_z\rangle$ basis are:

368
$$H_{CF} = D \begin{bmatrix} 1 & 0 & 0 & 0 & 5 \\ 0 & -4 & 0 & 0 & 0 \\ 0 & 0 & 6 & 0 & 0 \\ 0 & 0 & 0 & -4 & 0 \\ 5 & 0 & 0 & 0 & 1 \end{bmatrix} + d \begin{bmatrix} -2 & 0 & 0 & 0 & 0 \\ 0 & 1 & 0 & 0 & 0 \\ 0 & 0 & 2 & 0 & 0 \\ 0 & 0 & 0 & 1 & 0 \\ 0 & 0 & 0 & 0 & -2 \end{bmatrix}$$

369
$$\begin{bmatrix} 1 & 0 & 0 & 0 & 5 \\ 0 & -4 & 0 & 0 & 0 \\ 0 & 0 & 6 & 0 & 0 \\ 0 & 0 & 0 & -4 & 0 \\ 5 & 0 & 0 & 0 & 1 \end{bmatrix} + d \begin{bmatrix} -2 & 0 & 0 & 0 & 0 \\ 0 & 1 & 0 & 0 & 0 \\ 0 & 0 & 2 & 0 & 0 \\ 0 & 0 & 0 & 1 & 0 \\ 0 & 0 & 0 & 0 & -2 \end{bmatrix}$$

370 where $D = \frac{U_{3,2,4}}{6}$, $d = \frac{U_{3,2,2}}{7} \frac{6(a-c)}{R}$ are the corresponding energy scales of the base and perturbed crystal
 371 fields.

372
 373 Diagonalizing the Hamiltonian, without the spin-orbit contribution, and solving for eigenvalues,
 374 eigenvectors yields to first order the e_g , t_{2g} orbitals again, with distortion terms d splitting the degeneracy.
 375 The wavefunctions are given below in Table 5. Importantly, these wavefunctions are all subject to orbital
 376 quenching, in which the total angular momentum of each real wavefunction is zero. Consideration of spin-
 377 orbit terms below partially undo this quenching, which will give rise to the magnetocrystalline anisotropy
 378 observed in the NCO.

379
 380 Finally, the effect of exchange interaction is modeled using the tensor product of 5x5 identity matrix with
 381 the corresponding x, y, z Pauli spin matrices: $S_{x,y,z} = \sigma_{x,y,z} \otimes I_5$.

382

383 **Table S5: Solutions to Hamiltonian, neglecting spin-orbit coupling terms.**

State	Real Wavefunction	Wavefunction in $ L_z, S_z\rangle$ basis	Energy
φ_1	$ z^2, \uparrow\rangle$	$ 0, \uparrow\rangle$	$A + D + 2d$
φ_2	$ xy, \uparrow\rangle$	$\frac{1}{\sqrt{2}}(2, \uparrow\rangle - -2, \uparrow\rangle)$	$A - 2d$
φ_3	$ x^2 - y^2, \uparrow\rangle$	$\frac{1}{\sqrt{2}}(2, \uparrow\rangle + -2, \uparrow\rangle)$	$A + D - 2d$
φ_4	$ xy, \uparrow\rangle$	$\frac{1}{\sqrt{2}}(1, \uparrow\rangle + -1, \uparrow\rangle)$	$A + d$
φ_5	$ yz, \uparrow\rangle$	$\frac{1}{\sqrt{2}}(1, \uparrow\rangle - -1, \uparrow\rangle)$	$A + d$
φ_6	$ z^2, \downarrow\rangle$	$ 0, \downarrow\rangle$	$D + 2d$
φ_7	$ xy, \downarrow\rangle$	$\frac{1}{\sqrt{2}}(2, \downarrow\rangle - -2, \downarrow\rangle)$	$-2d$
φ_8	$ x^2 - y^2, \downarrow\rangle$	$\frac{1}{\sqrt{2}}(2, \downarrow\rangle + -2, \downarrow\rangle)$	$D - 2d$
φ_9	$ xy, \downarrow\rangle$	$\frac{1}{\sqrt{2}}(1, \downarrow\rangle + -1, \downarrow\rangle)$	d
φ_{10}	$ yz, \downarrow\rangle$	$\frac{1}{\sqrt{2}}(1, \downarrow\rangle - -1, \downarrow\rangle)$	d

384

385

386 II: Spin-orbit Contribution

387

388 Using the quantum state basis of $|L_z, S_z\rangle$ with $L_z \in \pm 2, \pm 1, 0$ in the d-orbitals, and $S_z \in \uparrow, \downarrow$ for spin-up and
 389 spin-down states, respectively, the effect of spin-orbit coupling term $\xi \vec{L} \cdot \vec{S} = \xi \left(L_z S_z + \frac{1}{2} (L_+ S_- + L_- S_+) \right)$
 390 in terms of raising and lowering operators gives the interaction matrix in the z-basis:
 391

392

$$H_{so,z} = \xi \begin{bmatrix} 1 & 0 & 0 & 0 & 0 & 0 & 0 & 0 & 0 & 0 \\ 0 & \frac{1}{2} & 0 & 0 & 0 & 1 & 0 & 0 & 0 & 0 \\ 0 & 0 & 0 & 0 & 0 & 0 & \frac{\sqrt{6}}{2} & 0 & 0 & 0 \\ 0 & 0 & 0 & -\frac{1}{2} & 0 & 0 & 0 & \frac{\sqrt{6}}{2} & 0 & 0 \\ 0 & 0 & 0 & 0 & -1 & 0 & 0 & 0 & 1 & 0 \\ 0 & 1 & 0 & 0 & 0 & -1 & 0 & 0 & 0 & 0 \\ 0 & 0 & \frac{\sqrt{6}}{2} & 0 & 0 & 0 & -\frac{1}{2} & 0 & 0 & 0 \\ 0 & 0 & 0 & \frac{\sqrt{6}}{2} & 0 & 0 & 0 & 0 & 0 & 0 \\ 0 & 0 & 0 & 0 & 1 & 0 & 0 & 0 & \frac{1}{2} & 0 \\ 0 & 0 & 0 & 0 & 0 & 0 & 0 & 0 & 0 & 1 \end{bmatrix}$$

393

394

Spin-orbit interaction matrix in the x-basis is formed by normal quantum mechanical coordinate transformation in terms of the already determined z-basis matrix. Explicitly:

395

396

397

$$H_{so,x} = \xi \begin{bmatrix} 0 & 0 & 0 & \frac{\sqrt{3}}{2} & 0 & 0 & 0 & 0 & 0 & -\frac{\sqrt{3}}{2} \\ 0 & 0 & 0 & 0 & \frac{1}{2} & 0 & 0 & 1 & \frac{1}{2} & 0 \\ 0 & 0 & 0 & \frac{1}{2} & 0 & 0 & 1 & 0 & 0 & \frac{1}{2} \\ \frac{\sqrt{3}}{2} & 0 & \frac{1}{2} & 0 & 0 & 0 & -\frac{1}{2} & 0 & 0 & \frac{1}{2} \\ 0 & \frac{1}{2} & 0 & 0 & 0 & \frac{\sqrt{3}}{2} & 0 & -\frac{1}{2} & \frac{1}{2} & 0 \\ 0 & 0 & 0 & 0 & \frac{\sqrt{3}}{2} & 0 & 0 & 0 & -\frac{\sqrt{3}}{2} & 0 \\ 0 & 0 & 1 & -\frac{1}{2} & 0 & 0 & 0 & 0 & 0 & -\frac{1}{2} \\ 0 & 1 & 0 & 0 & -\frac{1}{2} & 0 & 0 & 0 & -\frac{1}{2} & 0 \\ 0 & \frac{1}{2} & 0 & 0 & \frac{1}{2} & -\frac{\sqrt{3}}{2} & 0 & -\frac{1}{2} & 0 & 0 \\ -\frac{\sqrt{3}}{2} & 0 & \frac{1}{2} & \frac{1}{2} & 0 & 0 & -\frac{1}{2} & 0 & 0 & 0 \end{bmatrix}$$

398

399

400

401

402

403

Exact solutions of the full Hamiltonian are cumbersome, and we resort to the aforementioned numerical methods in general. Since the scale of spin-orbit coupling energy is small, a reasonable approximation can be obtained by treating SO coupling as a perturbation to the zeroth-order solutions in Table S6. Standard uses of degenerate and non-degenerate perturbation theory are necessary to approximate the perturbed states and energies. A summary of approximate states and energies along z, x directions are listed below.

404 **Table S6: summary of perturbed energies of real eigenstates. Difference between E_z , E_x energies leads**
 405 **to preferential spin-alignment, and thus the anisotropy of magnetization.**

State	Real State	Unperturbed Energy	E_z Perturbation	E_x Perturbation
φ_1	$ z^2, \uparrow\rangle$	$A + D + 2d$	$\frac{3}{2}\xi^2 \frac{1}{A + D + d}$	$\frac{3}{4}\xi^2 \left(\frac{1}{D + d} + \frac{1}{A + D + d} \right)$
φ_2	$ xy, \uparrow\rangle$	$A - 2d$	$\xi^2 \left(\frac{1}{-D} + \frac{\frac{1}{2}}{A - 3d} \right)$	$\frac{3}{2}d + \frac{1}{2}\sqrt{9d^2 + \xi^2}$
φ_3	$ x^2 - y^2, \uparrow\rangle$	$A + D - 2d$	$\xi^2 \left(\frac{1}{D} + \frac{\frac{1}{2}}{A + D - 3d} \right)$	$\xi^2 \left(\frac{\frac{1}{4}}{A + D - 3d} + \frac{\frac{1}{4}}{D - 3d} + \frac{1}{A} \right)$
φ_4	$ xy, \uparrow\rangle$	$A + d$	$\frac{1}{2}\xi$	$\frac{1}{4}\xi \left(\frac{1}{A} + \frac{1}{A + 3d} - \frac{1}{D - 3d} - \frac{3}{D + d} \right)$
φ_5	$ yz, \uparrow\rangle$	$A + d$	$-\frac{1}{2}\xi$	$\frac{3}{2}d - \frac{1}{2}\sqrt{9d^2 + \xi^2}$
φ_6	$ z^2, \downarrow\rangle$	$D + 2d$	$\frac{3}{2}\xi^2 \frac{\frac{3}{2}}{-(A - D - d)}$	$\frac{3}{4}\xi^2 \left(\frac{1}{D - d} - \frac{1}{A - D - d} \right)$
φ_7	$ xy, \downarrow\rangle$	$-2d$	$\xi^2 \left(\frac{1}{-D} - \frac{\frac{1}{2}}{A + 3d} \right)$	$\frac{3}{2}d - \frac{1}{2}\sqrt{9d^2 + \xi^2}$
φ_8	$ x^2 - y^2, \downarrow\rangle$	$D - 2d$	$\xi^2 \left(\frac{1}{D} - \frac{\frac{1}{2}}{A - D + 3d} \right)$	$\xi^2 \left(\frac{\frac{1}{4}}{D - 3d} - \frac{\frac{1}{4}}{A - D + 3d} - \frac{1}{A - D} \right)$
φ_9	$ xy, \downarrow\rangle$	d	$-\frac{1}{2}\xi$	$d - \frac{1}{4}\xi^2 \left(\frac{1}{A - 3d} + \frac{1}{A} + \frac{3}{D - d} + \frac{1}{D - 3d} \right)$
φ_{10}	$ yz, \downarrow\rangle$	d	$\frac{1}{2}\xi$	$\frac{3}{2}d + \frac{1}{2}\sqrt{9d^2 + \xi^2}$

406

407

408 III: Numerical Method

409

410 In lieu of using perturbation theory, we used Python and pylab's computational package to diagonalize the
 411 Hamiltonian more generally. From this, the effect of strain is able to be more systematically tested based
 412 on relative displacements of the oxygen ligands in the T_d and O_h environments. For example, in octahedra
 413 the oxygen ligands are located at 6 positions relative to the center of the octahedron:
 414 $(\pm 1, 0, 0)$, $(0, \pm 1, 0)$, $(0, 0, \pm 1)$. Strain is modeled through small displacement δ such that strain is applied
 415 in the appropriate plane, e.g. strained (001) NCO films experience displacements to
 416 $(1 + \delta, 0, 0)$, $(-1 - \delta, 0, 0)$, $(0, 1 + \delta, 0)$, $(0, -1 - \delta, 0)$, $(0, 0, 1 + 2\delta)$, and $(0, 0, -1 - 2\delta)$, under the
 417 assumption that the octahedra remain volume-invariant under the strain.

418

419 Direction of the electron spins is affected using the exchange interaction term of the Hamiltonian,
 420 $g\hbar(\vec{S}_i \cdot \vec{B}) = g\hbar(S_x B_x + S_y B_y + S_z B_z)$, with S_i terms involving the Pauli spin matrices. Energies of the
 421 in-plane and out-of-plane spin directions are determined by diagonalizing the corresponding Hamiltonian,
 422 with the difference in energies being the anisotropy energy.

423

424 Matrix elements come directly from the crystal field matrix elements above (Equation S1), without regard
 425 for making symmetry arguments to determine which to measure. The effect of strain is linear in the
 426 difference between the c-axis expansion and the a-axis contraction like $d \sim \frac{U_{2,3,2}}{7} \frac{6(a-c)}{R}$. Numerical

427 calculations to perform integrals remove the need for symmetry analysis, making the job much easier. Then,
428 energies of the recombined states are calculated, and the cases between in-plane and out-of-plane energies
429 as a function of δ can be compared, as shown in Fig. 4(c).

430

431

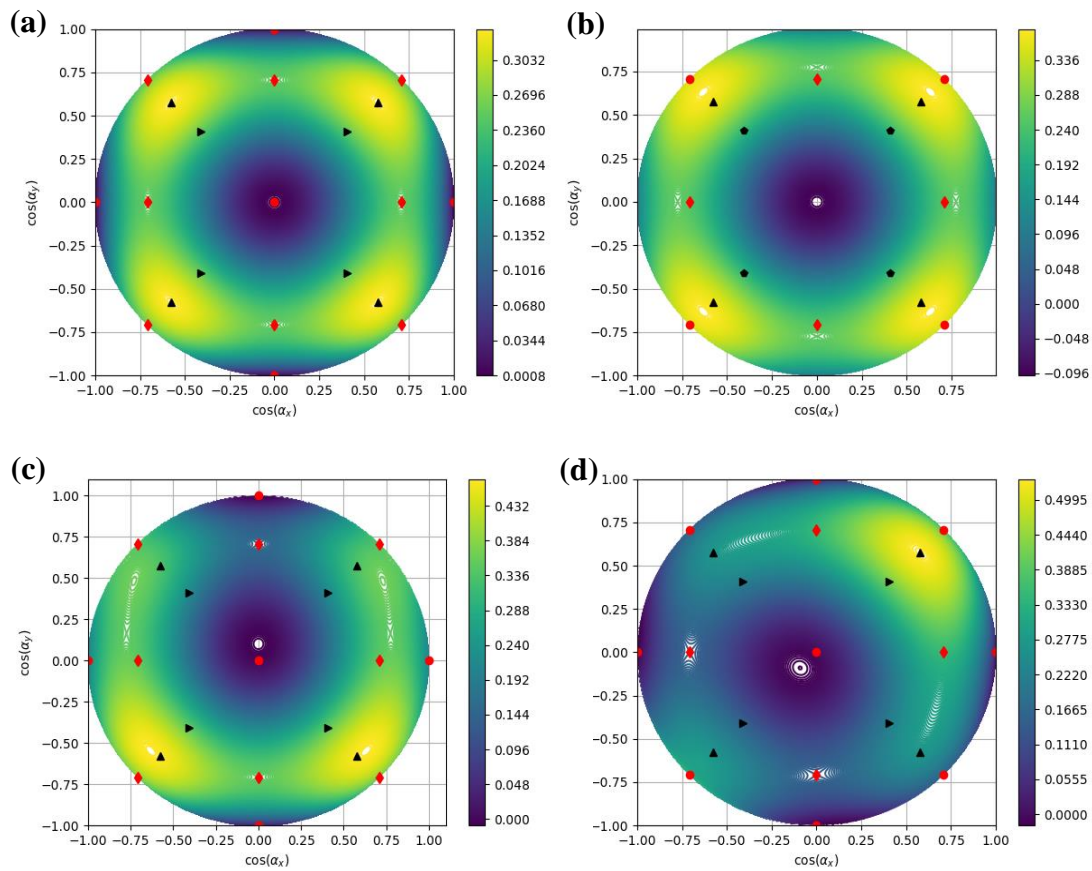
432 **References:**

433

434 [1] J. Inoue, T. Niizeki, H. Yanagihara, H. Itoh, and E. Kita, AIP Adv. **4**, 027111 (2014).

435 [2] K. Sato, Jpn. J. Appl. Phys. **20**, 2403 (1981).

436



437
 438 **Figure S4 | Single ion anisotropy simulation results.** Energy landscape solutions to the single-ion Hamiltonian,
 439 plotted as function of magnetization directions α_x , α_y . **(a)** is the unstrained Hamiltonian solution; **(b)-(d)** are the 0.3%
 440 compressively strained landscapes for strains in the (001), (110), and (111) crystal planes, respectively.